Electronic Supplementary Material (ESI) for Energy & Environmental Science.

Supplementary Information

Scalable production of an intermetallic Pt-Co electrocatalyst for high-power proton-exchange-membrane fuel cell

Tae Yong Yoo[1,2,†], Jongmin Lee[1,2,†], Sungjun Kim[1,2,†], Min Her[1,2], Shin-Yeong Kim[1,2], Young-Hoon Lee[1,2], Heejong Shin[1,2], Hyunsun Jeong[1,2], Arun Kumar Sinha[1,2], Sung-Pyo Cho[3], Yung-Eun Sung[1,2,*], Taeghwan Hyeon[1,2,*]

[1]*Center for Nanoparticle Research, Institute for Basic Science (IBS), Seoul 08826, Republic of Korea*

[2]*School of Chemical and Biological Engineering, and Institute of Chemical Processes, Seoul National University, Seoul 08826, Republic of Korea*

[3]*National Center for Inter-University Research Facilities, Seoul National University, Seoul 08826, Republic of Korea*

[†]These authors contributed equally to this work.
*To whom correspondences should be addressed.

E-mail: *ysung@snu.ac.kr* and *thyeon@snu.ac.kr*

Experimental Section

Materials

Cobalt (II) acetylacetonate ($Co(C_5H_7O_2)_2$, ≥ 99.0%), 2,2′-bipyridine (bpy, ≥ 99%), chloroplatinic acid hexahydrate ($H_2PtCl_6 \cdot 6H_2O$, ≥ 37.50% Pt basis), and perchloric acid ($HClO_4$, 70%) were purchased from Sigma-Aldrich. Ethanol (anhydrous, 99.9%), and isopropanol (99.5%) were purchased from Samchun Chemical. Ketjenblack EC-600JD (KB) was purchased from LION. All the chemicals were used without further purification. Ultrapure de-ionized (DI) water (Milli-Q, resistivity of 18.2 MΩ, total organic carbon of 2 ppb) was used for the synthesis of i-CoPt/KB and the preparation of electrolytes.

Synthesis of $[Co(bpy)_3][PtCl_6]$ compound (Co-Pt compound)

Co-Pt compound was prepared simply by addition of $[PtCl_6]^{2-}$ complex solution into $[Co(bpy)_3]^{2+}$ complex solution. 2 mmol of $Co(C_5H_7O_2)_2$ (or one of $CoCl_2$, $Co(NO_3)_2$, $CoSO_4$, and $Co(CH_3CO_2)_2$) was immersed in 20 mL of DI water and 6 mmol of bpy was dissolved in 20 mL of ethanol (99.9%), separately. These two solutions were mixed together and stirred for 24 hrs at room temperature to obtain the $[Co(bpy)_3]^{2+}$ complex solution. $[PtCl_6]^{2-}$ complex solution was obtained by dissolving 2 mmol of $H_2PtCl_6 \cdot 6H_2O$ in 40 mL of ethanol (99.9%). Bright yellow Co-Pt compound precipitated upon addition of $[PtCl_6]^{2-}$ complex solution into $[Co(bpy)_3]^{2+}$ complex solution. Co-Pt compound could easily settle upon 3 mins of centrifugation at 10,000 rpm. After several washing steps of Co-Pt compound with ethanol, the powder was dried in an oven at 50 °C overnight.

Synthesis of i-CoPt/KB and i-CoPt@Pt/KB

In a typical synthesis, 750 mg of Co-Pt compound and 210 mg of KB were ground together in a mortar to obtain a composite. We could get a better quality of composite by a mild ball milling (10 mins at 400 rpm) with addition of a proper amount of ethanol. The composite was thermally annealed at 900 °C for 6 hrs under vacuum (0.5-1 10^{-2} Torr) to obtain i-CoPt/KB. Inert gases such as Ar caused a segregation of the Co monometallic phase, which reduced the extent of alloying between Pt and Co, and caused the severe dissolution of Co under fuel cell operating condition. i-CoPt@Pt/KB was prepared by sequential treatments that include air etching (2 hrs at 200 °C in a muffle furnace), H_2-annealing (2 hrs at 600 °C in an Ar flow of 150 sccm with 5% H_2), and acid treatment (12 hrs stirring in 0.1 M $HClO_4$ at 70 °C).

Characterization

Scanning electron microscopy (SEM) measurements with energy-dispersive spectroscopy (EDS) were conducted using SUPRA 55VP (Carl Zeiss) and JSM-7800F Prime (JEOL Ltd., Japan) instruments. Transmission electron microscopy (TEM) and scanning transmission electron microscopy (STEM) measurements with energy-dispersive spectroscopy (EDS) were conducted on a JEOL EM-2010 microscope operated at 200 kV. X-ray diffraction (XRD) patterns were acquired on a Rigaku SmartLab X-ray diffractometer using Cu Kα radiation. High-angle annular dark-field scanning transmission electron microscopy (HAADF-STEM) measurements were conducted using a JEM-ARM200F (Cold FEG, JEOL Ltd., Japan) model instrument at the National Center for Inter-University Research Facilities (Seoul National University) with an acceleration voltage of 200 kV. X-ray photoelectron spectroscopy (XPS) measurements were conducted in both lab-source instrument and synchrotron-based facilities.

For the lab-source analysis, the K-Alpha$^+$ XPS system (Thermo Fisher Scientific) was used with the energy source of microfocused monochromated Al-K$_a$ (1486.6 eV). Synchrotron-based analysis was performed at Beamline 8A1 of Pohang Accelerator Laboratory (PAL). Incident photon energy was varied by controlling the gap of undulator and calibrated using gold foil which has Au 4f$_{7/2}$ spectrum peak at 84.0 eV of binding energy. Fourier transform infrared spectroscopy (FTIR) was conducted on a TENSOR27 model instrument (Bruker, Germany) in ATR mode with a spectral range from 4,000 to 400 cm^{-1}. Inductively coupled plasma atomic emission spectroscopy (ICP-AES) analyses were performed using OPTIMA 8300 (Perkin-Elmer, USA) model instrument at the National Center for Inter-University Research Facilities. X-ray absorption near edge structure (XANES) and extended X-ray absorption fine structure (EXAFS) analyses were conducted at Beamline 10C of PAL. The Si(111) crystal was used as a monochromator and the incident beam was calibrated before the measurement using Pt and Co foils. All samples were densely packed in powder form at each optimized thickness and were analyzed under ambient condition. Brunauer-Emmett-Teller (BET) nitrogen adsorption-desorption isotherm and Barrett-Joyner-Halenda (BJH) pore-size distribution analyses were conducted on a BELSORP-MAX (MicrotracBEL, Corp., Japan) with N_2 gas at 77 K. The acquired data were normalized by pure carbon weight of the samples.

Electrochemical measurements

The electrochemical measurements of the catalysts were conducted using the rotating-disk electrode (RDE) setup with a modulated speed rotator (PINE, AFMSRCE) and a potentiostat (Autolab, PGSTAT 302N). To prevent the crossover of anion species from the reference electrode, such as chloride that causes the blocking of Pt surface, we used a home-made fluorinated ethylene propylene (FEP) cell with a salt-bridge. All measurements were conducted after an acid treatment and three times of boiling in DI water to remove any possible impurities in FEP cell. Glassy carbon (GC) electrode (PINE, disk area of 0.2475 cm^2), Ag/AgCl (BASi, 3M NaCl) and graphite carbon rod (Alfa-Aesar) were used as working, reference, and counter electrodes, respectively. The inks were prepared by dispersing each catalyst (5 mg) in a mixture of DI water and isopropanol (2.5 mL) and Nafion ionomer (40 μL, Sigma-Aldrich, 5 wt %) by ultrasonication. For commercial Pt/C (Johnson Matthey Co., 20 wt %), 20 μL of Nafion ionomer was used for the ink preparation. The inks were drop casted on the GC disk and evaporated while rotating the disk at 600 rpm to prepare uniform films of catalysts. The Pt loadings were set to 15 μg_{Pt} cm^{-2} for all the catalysts. All potentials below were referenced to a reversible hydrogen electrode (RHE).

The electrolyte was 0.1 M $HClO_4$ (Sigma-Aldrich, 70%) and all the RDE measurements were conducted at room temperature. Before ORR measurement, the catalysts were pretreated in Ar-saturated electrolyte in the potential between 0.05 and 1.05 V (versus RHE) at a scan rate of 50 mV s^{-1} until stable voltammogram curves were attained. The cyclic voltammogram (CV) curves of the pretreated catalysts were obtained in a fresh Ar-saturated electrolyte in the potential between 0.05 and 1.1 V (versus RHE) at a scan rate of 20 mV s^{-1}. For oxygen reduction reaction (ORR) measurement, the pretreated catalysts were transferred to a fresh O_2-saturated electrolyte and polarized between 0.05 and 1.1 V (versus RHE) at a scan rate of 20 mV s^{-1} with a rotating speed of 1600 rpm. The in situ iR-drop compensation was applied during ORR measurement with the solution resistance value.

The intrinsic ORR polarization curves were obtained by subtraction of the CV curves from the ORR curves. The kinetic current density (J_k) was obtained by the Koutecký-Levich equation:

$J_k = J \times J_L/(J-J_L)$, and the Pt mass activity (A mg_{Pt}^{-1}) was calculated from the kinetic current density at 0.9 V (versus RHE) normalized by the Pt loading (μg_{Pt} cm^{-2}).

For electrochemical surface area (ECSA) measurement, the conventional hydrogen underpotential deposition (H_{upd}) and CO stripping methods were performed. ECSA derived from H_{upd} was calculated by the equation: ECSA (m^2 g_{Pt}^{-1}, H_{upd}) = $Q_{Pt}/0.21 \times L_{Pt}$, where Q_{Pt} and L_{Pt} represent the charge density (C cm^{-2}) of proton adsorption and Pt loading (μg_{Pt} cm^{-2}), respectively. For CO stripping, each catalyst was first pretreated in Ar-saturated electrolyte and transferred to a fresh Ar-saturated electrolyte. With potential holding at 0.05 V (versus RHE), the electrolyte was purged with CO gas for 5 mins and subsequently purged with Ar gas for 30 mins to remove CO molecules in the electrolyte. Then CV curve was obtained between 0.05 and 1.1 V (versus RHE) at a scan rate of 20 mV s^{-1}. ECSA derived from CO stripping was calculated by the equation: ECSA (m^2 g_{Pt}^{-1}, CO stripping) = $R_{Pt}/0.42 \times L_{Pt}$, where R_{Pt} represents the charge density (C cm^{-2}) of CO stripping. CO stripping charge was obtained from the difference between CO stripping and CV curve.

The accelerated durability test (ADT) was carried out by cycling the working electrode between 0.6 and 1.0 V for 30,000 cycles in O_2-saturated 0.1 M $HClO_4$.

For rotating ring-disk electrode (RRDE) measurements to obtain the electron transfer number during ORR, the GC disk electrode with Pt ring (PINE, disk area of 0.1963 cm^2) was used. The potential of the Pt ring was set to 1.2 V (versus RHE) during ORR measurements for the oxidation of H_2O_2. The electron transfer number was calculated from the disk current (I_d) and ring current (I_r) using the equation: Electron transfer number (n) = $4 \times (I_d/(I_d + I_r/NC))$, where NC represents the collection efficiency of the RRDE electrode.

Membrane electrode assembly (MEA) fabrication

The MEAs for single cell tests were fabricated by catalyst-coated membrane (CCM) method. 25 μm Nafion 211 membrane was used as a proton exchange membrane, and the membrane was pre-boiled by immersing it in DI water at 80 ℃ for 1 hr. Commercial 40 wt % Pt/C (HiSPEC 4000, Johnson Matthey Co.) and the prepared i-CoPt@Pt/KB were used for anode and cathode, respectively. Catalyst slurries were prepared by dispersing the catalysts with perfluorosulfonic acid (PFSA) ionomer (Aquivion D83-06A, 6 wt % ionomer solution in low aliphatic alcohols and water) in an aqueous solution of isopropanol, and ultrasonicating for more than 30 mins to obtain a homogeneous dispersion. The ionomer to carbon weight ratios of the Pt/C and i-CoPt@Pt/KB at cathode were optimized to 0.5 and 0.8, respectively. The prepared slurries were directly sprayed onto the pre-boiled Nafion 211 membrane, and the Pt loadings for both electrodes were fixed at 0.1 $\mathrm{mg_{Pt}\ cm^{-2}}$ with an active area of 5 $\mathrm{cm^2}$ (**Figure S45**). After the catalyst layer coating process, the prepared CCM was dried at room temperature for more than 12 hrs to evaporate residual alcohol solvents in the catalyst layer. Afterwards, the CCM, two gas diffusion layers with a microporous layer (320 μm, JNT30-A6H, JNTG Co.), and two gaskets were pressed between two graphite plates with a one-channel serpentine flow field (2.2 cm x 2.3 cm) (**Figure S46**) by applying torque (8.5 N m) to each screw of the end plates. For the benchmark, the MEAs with cathodes using commercial Pt/C (40 wt % Pt on carbon black, HiSPEC 4000, Johnson Matthey Co.), commercial PtCo/C (46.5 wt % Pt, 4.7 wt % Co on high surface carbon, TEC36E52, TKK), and synthesized Pt/KB (40 wt % Pt on Ketjen Black) were also prepared using the same fabrication process. The ionomer to carbon weight ratios of each catalyst were optimized respectively. (0.5 for the commercial Pt/C, 0.8 for the commercial TKK PtCo/C and Pt/KB)

Single cell test and characterization

The prepared single cell was connected to a fuel cell test station (CNL Energy Co.) (**Figure S47**). Before the single cell test, the break-in procedure began by heating the cell and humidifiers to 80 °C and holding the cell at open circuit voltage (OCV) in H_2-O_2 condition. In the break-in process, fully humidified hydrogen and oxygen were fed to the anode and cathode at a constant flow rate of 0.2 L min^{-1}, respectively, without any back-pressure. After the set temperature was reached, the as-prepared MEAs were activated by repeatedly applying the current load in steps of 1.0 A cm^{-2} for 10 mins (in the range of OCV to 0.4 V) until the stabilized cell voltage was achieved at the corresponding discharge current load. After the break-in process, H_2-O_2 single-cell polarizations were obtained at 80 °C by supplying fully humidified H_2 (0.2 L min^{-1}) and O_2 (0.2 L min^{-1}) with a back pressure of 50 kPa (150 kPa_{abs}) to compensate the water vapor pressure. Then, electrochemical impedance spectroscopy (EIS, Zahner PP242) was conducted at 0.05 A cm^{-2} with an amplitude of 0.002 A cm^{-2} over the frequency range of 0.1 to 100 kHz at the H_2-O_2 condition to characterize the electrochemical properties of the tested MEAs. Next, H_2-air single cell test was conducted at 80 °C by supplying fully humidified H_2 (0.2 L min^{-1}) and air (0.8 L min^{-1}) at 100, 150, and 250 kPa_{abs}) to the anode and cathode, respectively. Electrochemical impedance spectroscopy (EIS) was conducted at various current densities (0.1, 0.4, 0.8, 1.2, 1.6, and 2.0 A cm^{-2}) with an amplitude of 5% of each operating current density over the frequency range of 1.0 to 100 kHz to characterize the electrochemical properties of the tested MEAs. After the single cell polarization test, the single cell was purged with fully humidified N_2 (0.2 L min^{-1}) for more than 12 hrs at room temperature. Cyclic voltammetry (CV) was conducted between 0.05 and 1.2 V at a scan rate of 100 mV s^{-1} at 30 °C to determine the ECSA of cathode catalysts in MEA configuration. Fully humidified hydrogen (0.2 L min^{-1}) and nitrogen (0.2 L min^{-1}) were fed to the anode and cathode, respectively. The ECSA of cathode catalysts was calculated by integrating the H_{upd} peak, assuming a value of 210 μC cm_{Pt}^{-2} for the adsorption of a hydrogen monolayer on Pt. H_2 crossover currents were measured by linear sweep voltammetry (LSV) under fully humidified H_2-N_2 condition (0.2 L min^{-1} at 150 kPa_{abs}) at 80 °C. The mass activity was calculated from the current density at 0.9 $V_{iR\text{-}corrected}$ with correction for measured H_2 crossover current (**Figure S48**). The ADT on the cathode in MEA was conducted using the square-wave potential cycling between 0.6 V (3 s) and 0.95 V (3 s) according to the US DOE ADT protocol under fully humidified H_2-N_2 condition (0.1/0.2 L min^{-1} at 150 kPa_{abs}) at 80 °C.

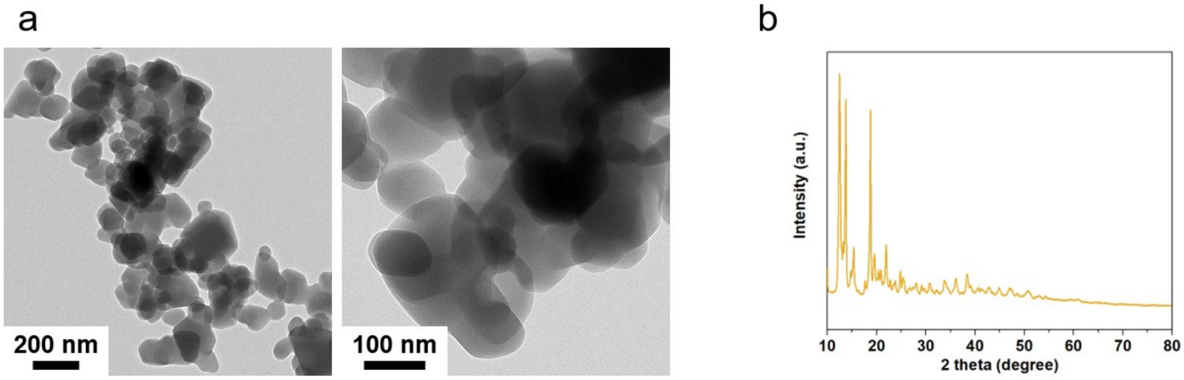

Figure S1. (a) TEM images and (b) XRD pattern of Co-Pt compound.

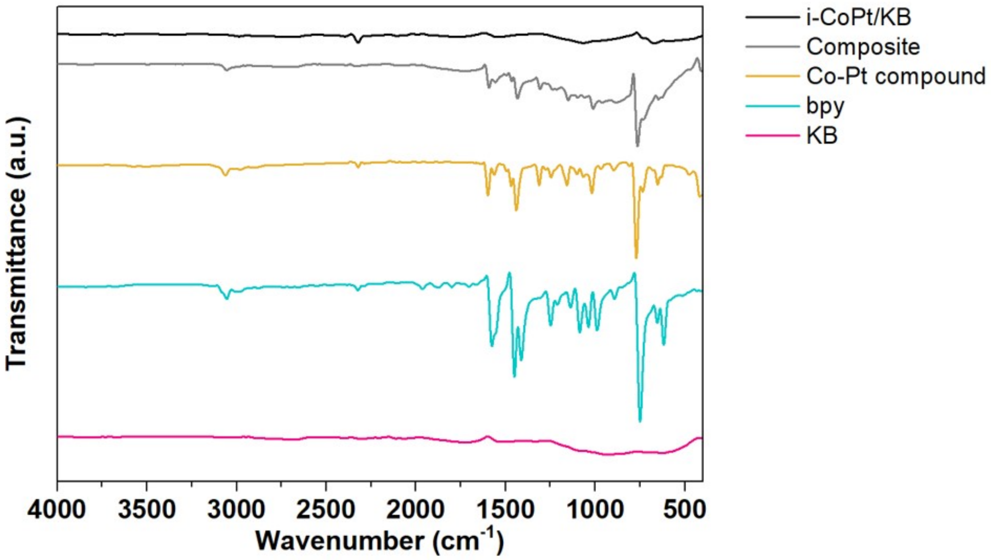

Figure S2. FTIR data of KB, bpy, Co-Pt compound, composite, and i-CoPt/KB.

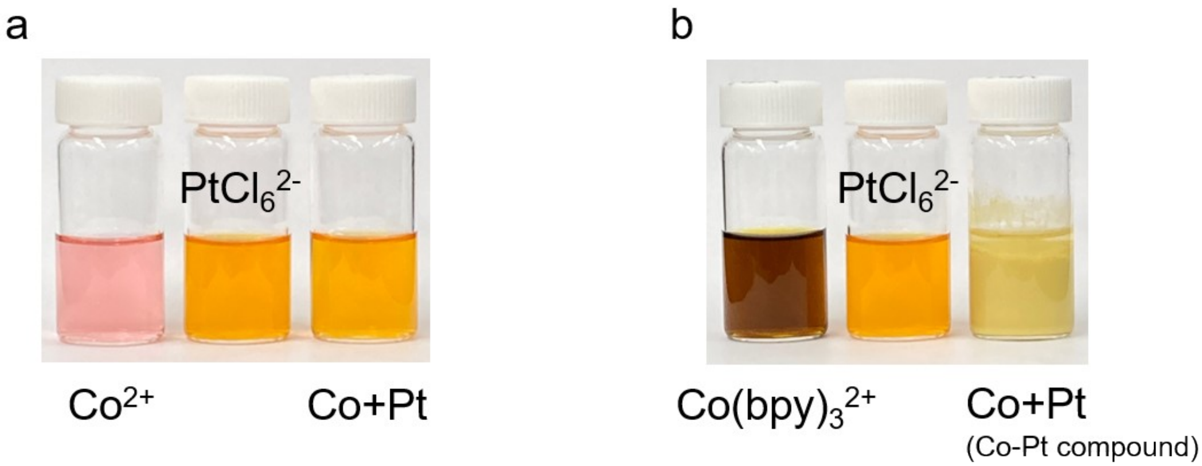

Figure S3. Mixtures of (a) Co^{2+} + $PtCl_6^{2-}$ and (b) $Co(bpy)_3^{2+}$ + $PtCl_6^{2-}$ (Co-Pt compound).

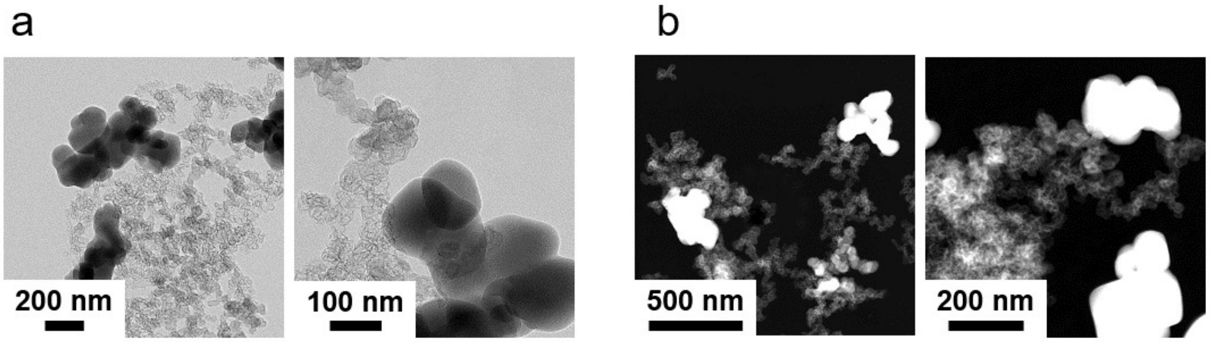

Figure S4. (a) TEM and (b) STEM images of composite.

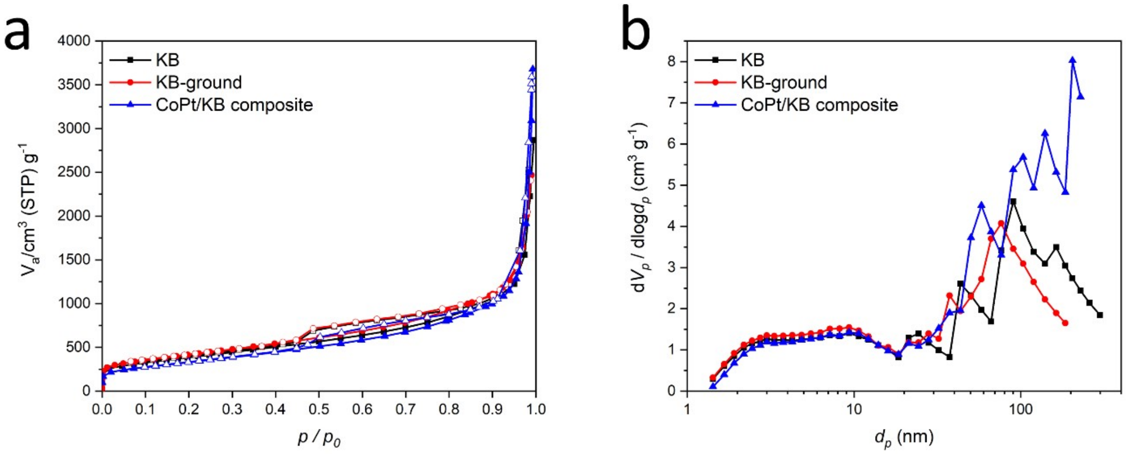

Figure S5. (a) BET nitrogen adsorption-desorption isotherm, and (b) BJH pore size distribution of KB, ground KB, and the ground composite (Co-Pt compound and KB).

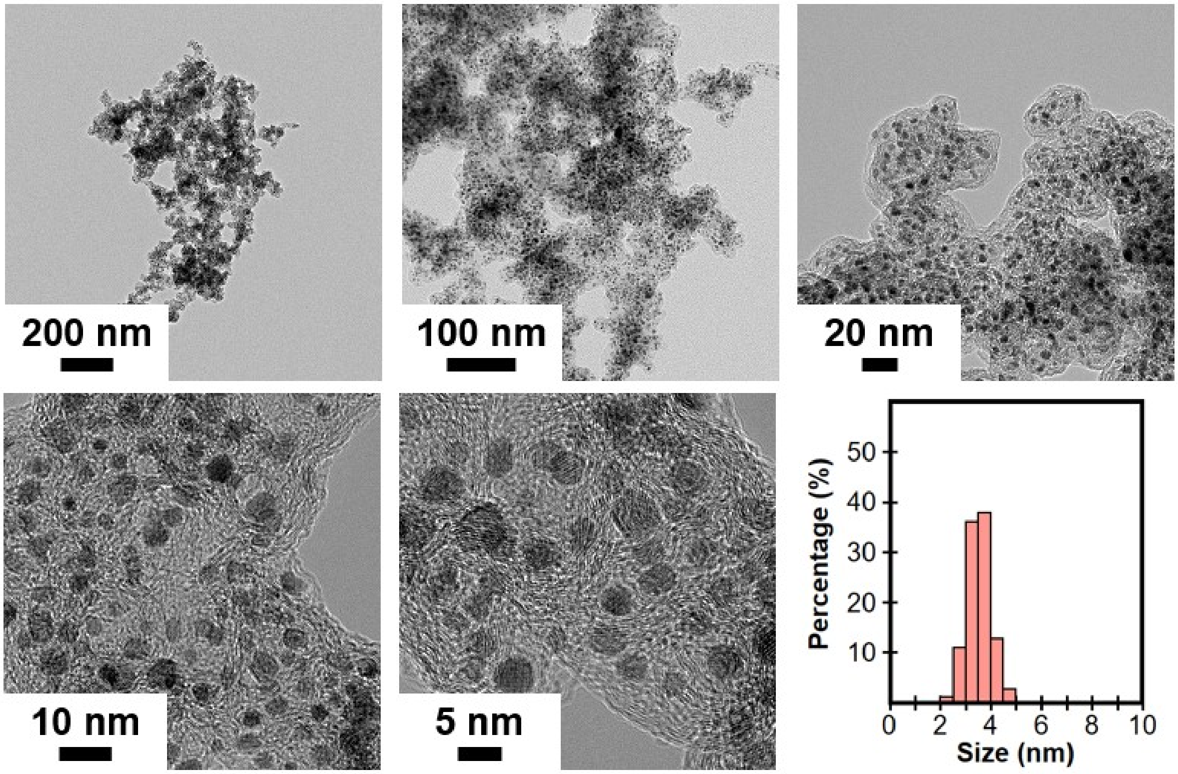

Figure S6. TEM images and the nanoparticle size distribution of i-CoPt/KB.

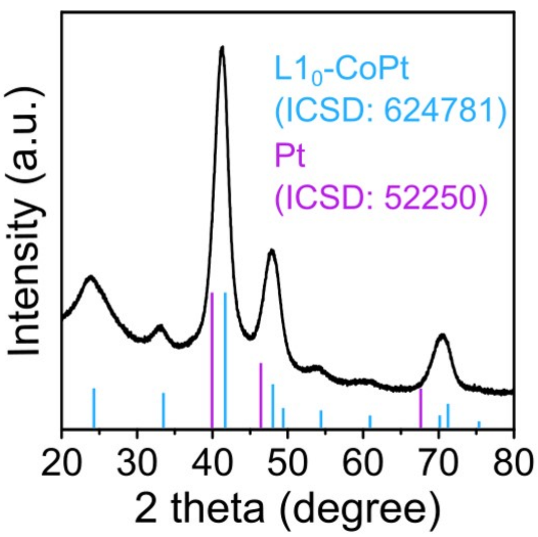

Figure S7. XRD pattern of i-CoPt/KB.

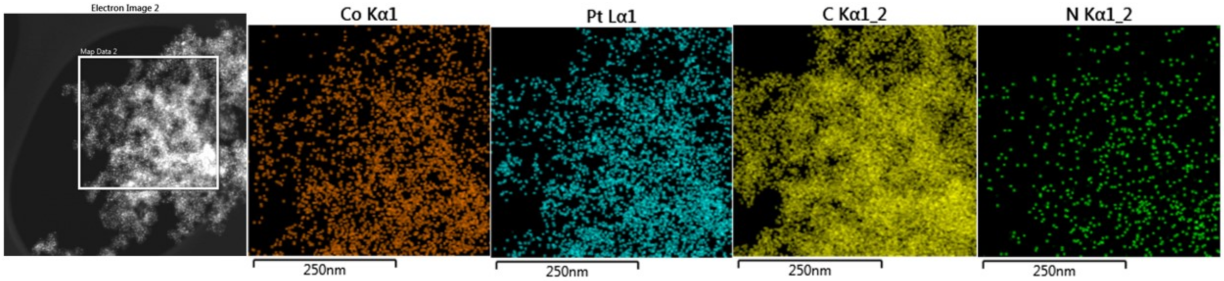

Figure S8. STEM-EDS mapping of i-CoPt/KB.

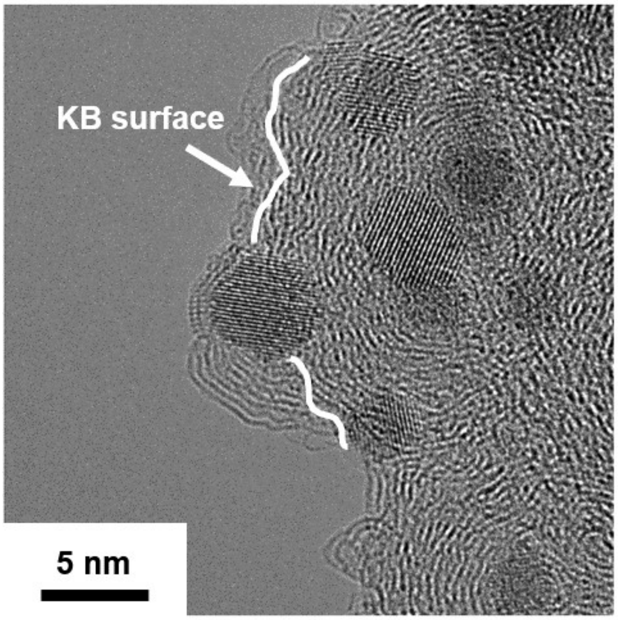

Figure S9. TEM image of N-doped carbon shells on i-CoPt nanoparticles in i-CoPt/KB.

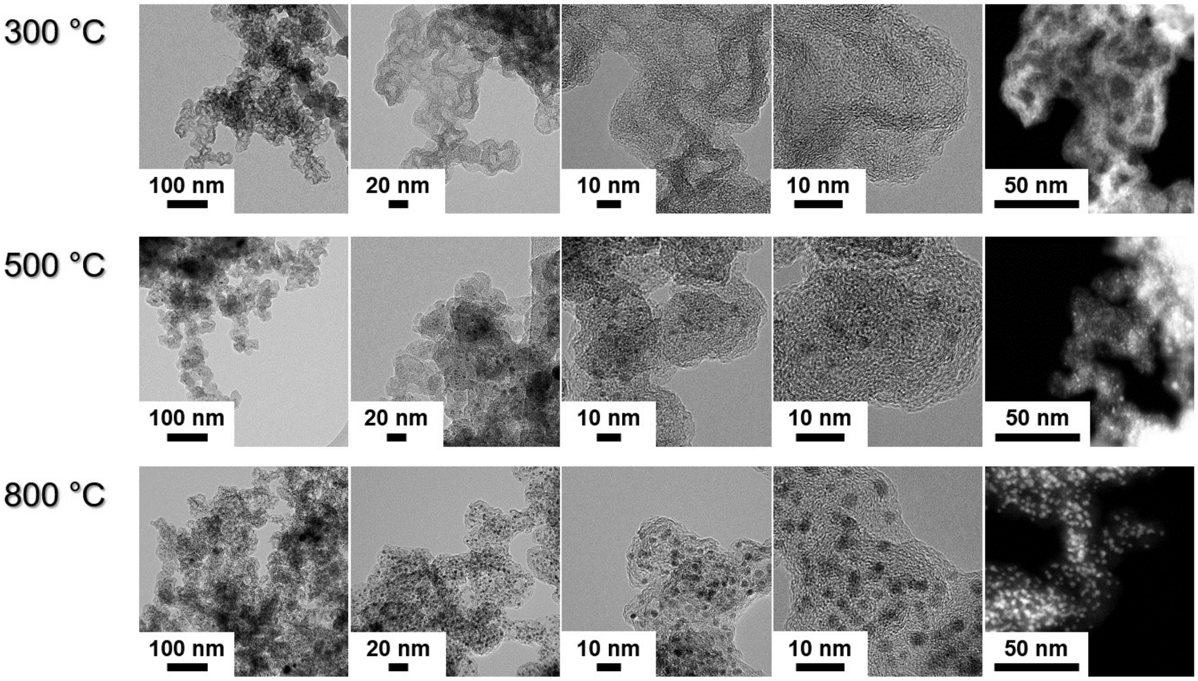

Figure S10. TEM and STEM images of 300, 500, and 800 °C *ex situ* samples. At 300 °C, KB is covered with a compound-derived carbon matrix, which contains Co and Pt species. We then observed a generation of Co_xPt_y and Co clusters at 500 °C, followed by a growth of particle sizes to 2-2.5 nm as the temperature increased to 800 °C.

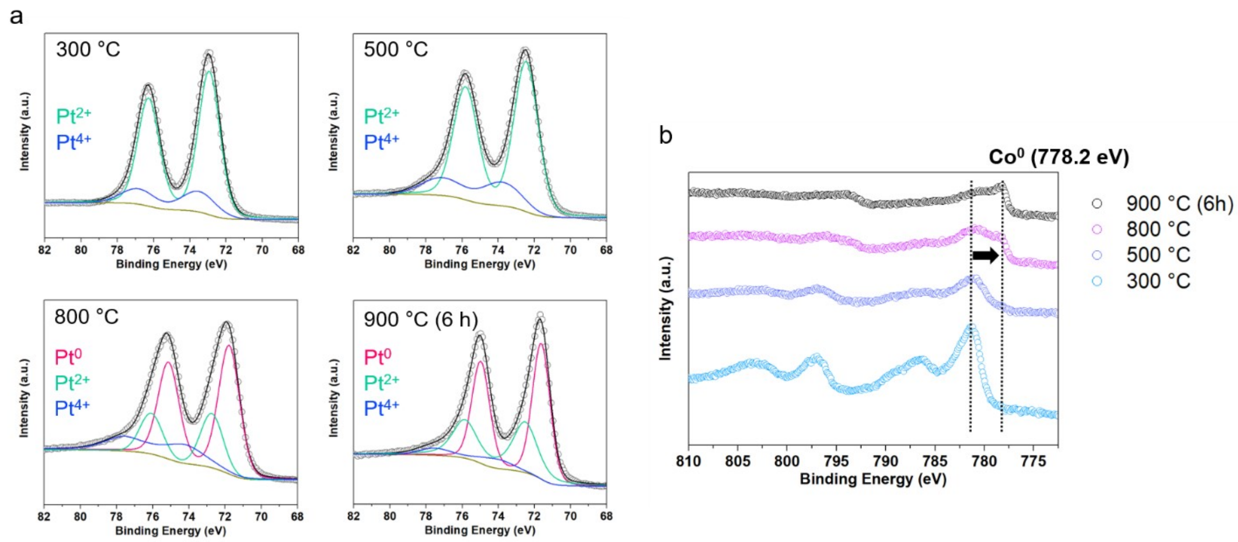

Figure S11. (a) XPS Pt 4f spectra of 300, 500, 800, and 900 °C (6 h) *ex situ* samples. At 300 and 500 °C, Pt remains completely oxidized due to its small particle sizes. As the temperature increased to 800 °C, we confirmed the significant portion of Pt^0 state, which slightly increased after 6 hrs at 900 °C. (b) XPS Co 2p spectra of 300, 500, 800, and 900 °C (6 h) *ex situ* samples. Up to 500 °C, Co remains oxidized due to its small particle sizes. As the temperature increased from 500 to 900 °C, we observed a significant increase in Co^0 state due to the alloying of Co with Pt.

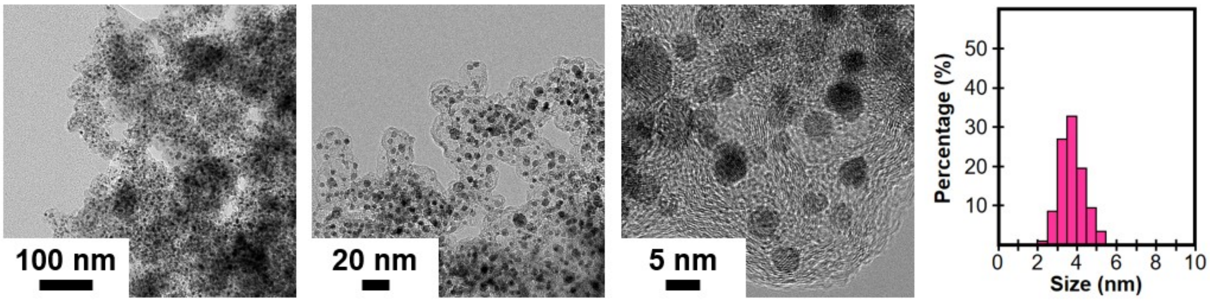

Figure S12. TEM images and the nanoparticle size distribution of i-CoPt@Pt/KB.

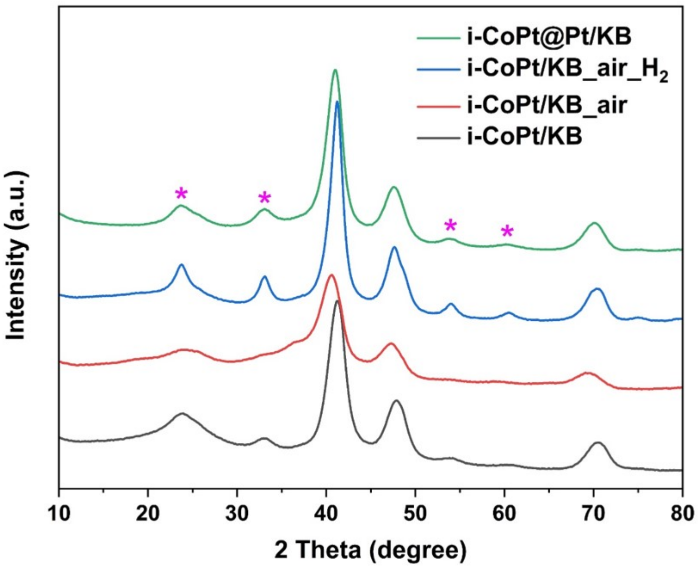

Figure S13. XRD pattern changes during activation process (asterisks at the characteristic peaks of intermetallic $L1_0$-CoPt).

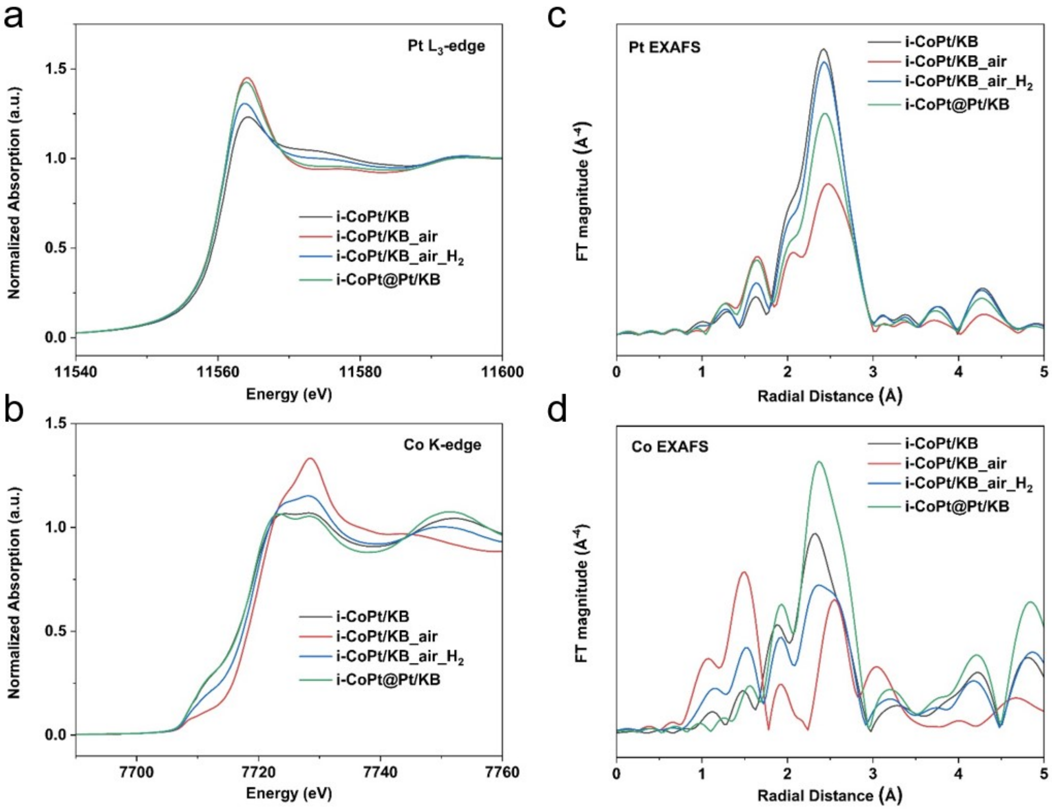

Figure S14. XANES spectra changes of (a) Pt L_3-edge and (b) Co K-edge, and EXAFS spectra changes of (c) Pt and (d) Co during activation process. The as-prepared i-CoPt/KB showed characteristic Pt-Co interaction peaks in Pt and Co XANES spectra.[1] After air etching (2 hrs at 200 °C), the white-line intensity of Pt XANES and the Pt-O coordination peak of Pt EXAFS increased simultaneously, which indicates that the N-doped carbon shell was effectively removed and the Pt surface was well exposed to the air. Similar trend was also observed for Co, which corroborates the formation of Co oxide species as confirmed in XPS analysis. We speculate that the unstable Co atoms on the surface of i-CoPt nanoparticles were oxidized during the air etching process, producing a thin layer of Co oxide on the surface of CoPt nanoparticles. Upon H_2-annealing (2 hrs at 600 °C), the Pt white-line intensity, and the coordination states of Pt-O and Co-O largely recovered to their initial states of i-CoPt/KB, which collectively indicate that the electronic interaction between Pt and Co became stronger in CoPt alloy by enhanced atomic ordering. However, Co XANES and EXAFS analyses identified the remaining Co oxide species in H_2-annealed sample that needs to be removed for a better proton conduction in ionomer. Upon acid treatment, the Co XANES curve of the activated i-CoPt@Pt/KB completely matched with that of the as-prepared i-CoPt/KB, and the Co-O coordination peak in Co EXAFS vanished in i-CoPt@Pt/KB. This indicates that the oxidized Co species on the surface of i-CoPt@Pt was totally removed and the internal i-CoPt core remained intact. On the other hand, Pt XANES spectrum of i-CoPt@Pt/KB showed increased white-line intensity compared to that of i-CoPt/KB, which demonstrates the fully exposed Pt-skin surface in i-CoPt@Pt/KB.

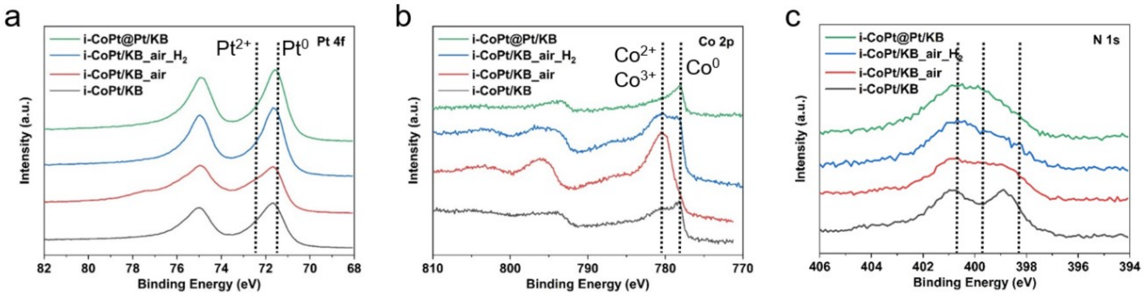

Figure S15. XPS (a) Pt 4f, (b) Co 2p, and (c) N 1s spectra changes during activation process. Upon air etching, N-doped carbon shells on i-CoPt nanoparticles were etched off, revealing the Pt surface and oxidizing unstable Co species. H_2-annealing effectively reduced both Co and Pt, facilitating the atomic arrangement between Co and Pt, but there still remained oxidized Co after H_2-annealing. Finally, acid treatment completely removed the oxidized Co species which can be dissolved during fuel cell operation to block proton conduction and cause Fenton reaction. We further confirmed the decrease in pyridinic-N (398.3 eV) and pyrrolic-N (399.7 eV), with increased proportion of graphitic-N (400.7 eV) after activation process, due to a higher stability of graphitic-N.[2]

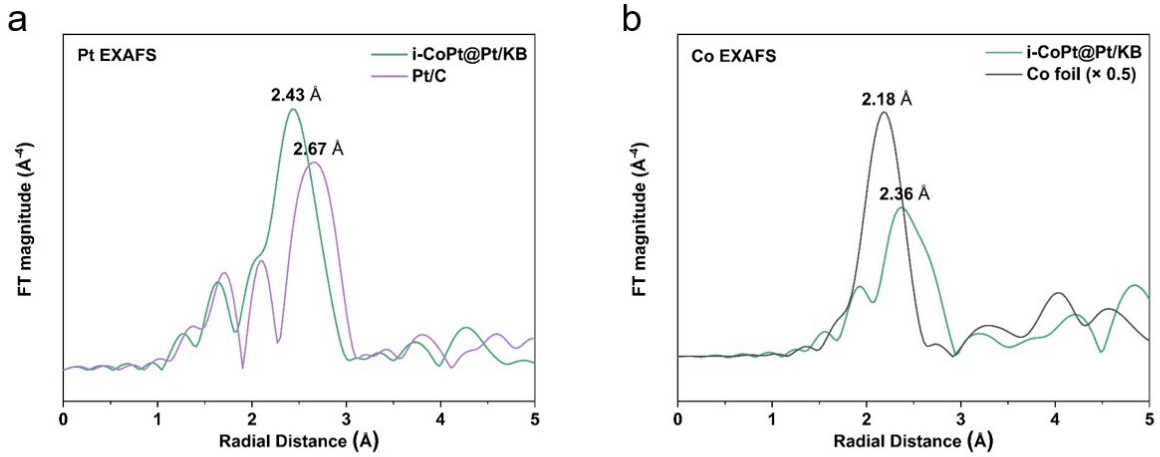

Figure S16. (a) Pt EXAFS compared to Pt/C, and (b) Co EXAFS compared to Co foil, respectively.

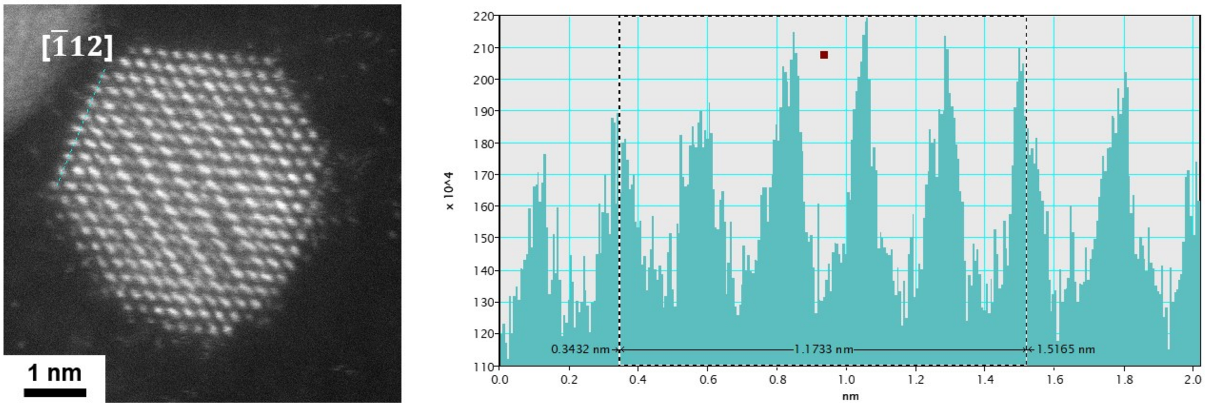

Figure S17. HAADF-STEM image of i-CoPt@Pt/KB (left), and the line profile of the outermost Pt surface for the lattice strain calculation along the [$\bar{1}12$] direction (right).

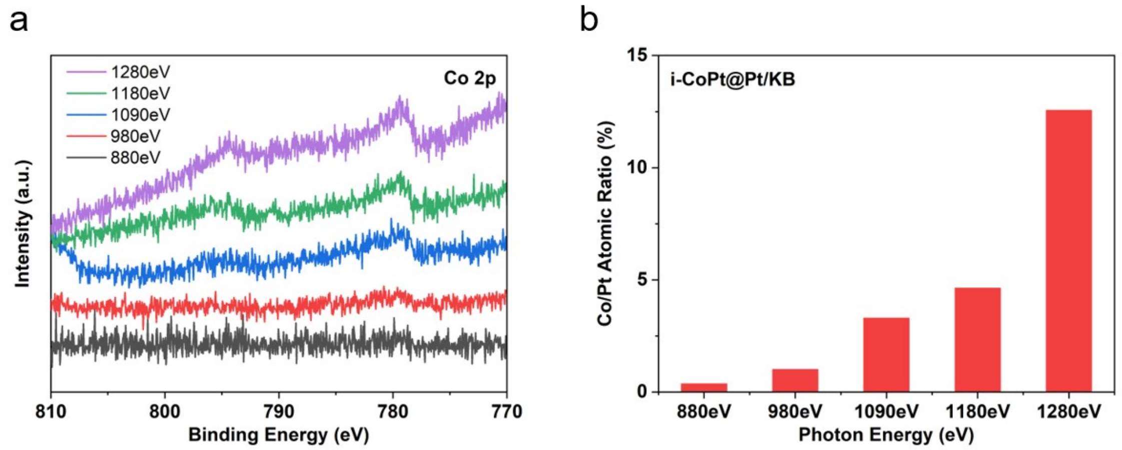

Figure S18. (a) Co 2p spectra and (b) Co/Pt ratio depending on the incident photon energy from 880 to 1280 eV. As the incident photon energy increases, the kinetic energy of photoelectron originated from Co 2p core level also increases. The kinetic energy of photoelectron is a key factor of probing depth since the escape depth of photoelectron depends on the kinetic energy. This means that the XPS results obtained at higher photon energy normally include more core-dependent information than surface information of the particle. From the increased signal of Co 2p at high photon energy, we confirmed that Co atoms are mostly located at the core of the nanoparticles, which corresponds to the i-CoPt@Pt structure.

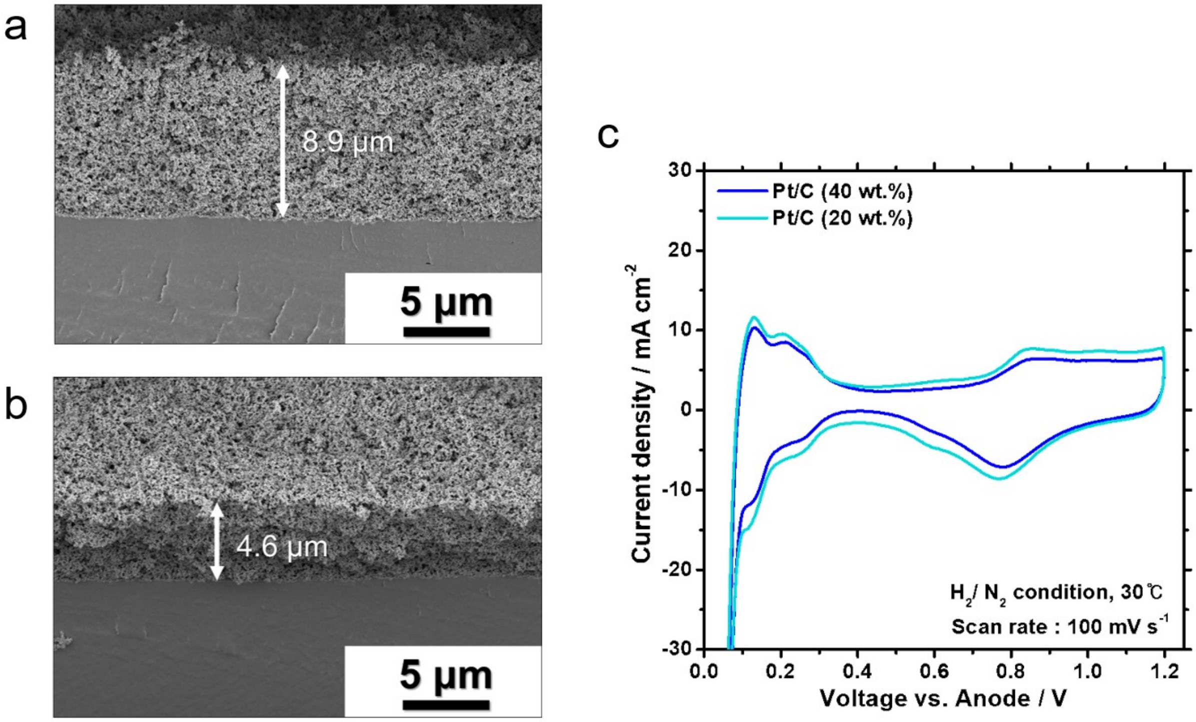

Figure S19. SEM cross-section images of CCLs made of (a) 20 and (b) 40 wt % Pt/C. (c) CV curves of the 20 and 40 wt % Pt/C. Test condition (H_2-N_2): 30 °C, 100% relative humidity, H_2 flow rate = 0.2 L min^{-1}, N_2 flow rate = 0.2 L min^{-1}.

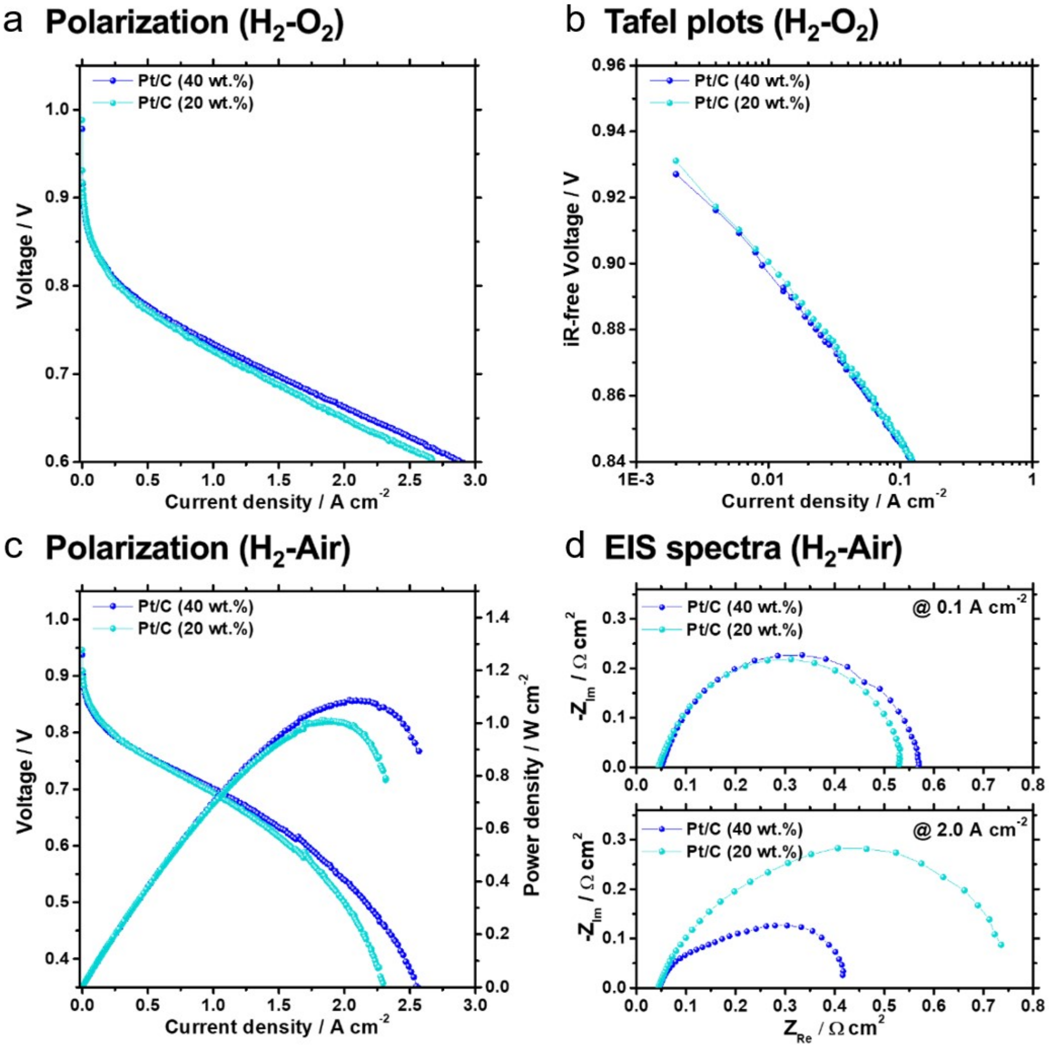

Figure S20. Single cell performance of the 20 and 40 wt % Pt/C under H_2-O_2 and H_2-air conditions. (a) H_2-O_2 fuel cell polarization curves, and (b) the derived Tafel plots before and after ADT cycling. Test condition (H_2-O_2): 80 °C, 100% relative humidity, H_2 flow rate = 0.2 L min^{-1} (150 kPa$_{abs}$), O_2 flow rate = 0.2 L min^{-1} (150 kPa$_{abs}$) (c) H_2-air fuel cell polarization curves, and (d) EIS spectra at 0.1 A cm^{-2} and 2.0 A cm^{-2}. Test condition (H_2-air): 80 °C, 100% relative humidity, H_2 flow rate = 0.2 L min^{-1} (250 kPa$_{abs}$), air flow rate = 0.8 L min^{-1} (250 kPa$_{abs}$).

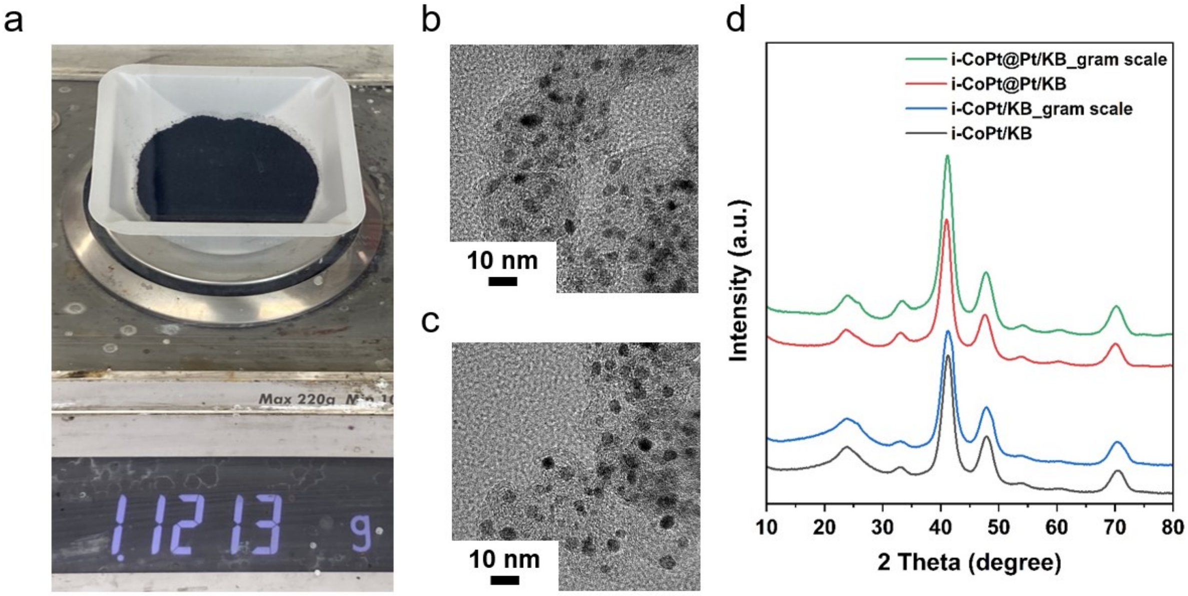

Figure S21. (a) Photograph of the gram-scale-synthesized i-CoPt/KB. TEM images of (b) the gram-scale-synthesized i-CoPt/KB and (c) its activated i-CoPt@Pt/KB. (d) XRD patterns of the gram-scale-synthesized i-CoPt/KB and its activated i-CoPt@Pt/KB compared to those of the typical synthesis.

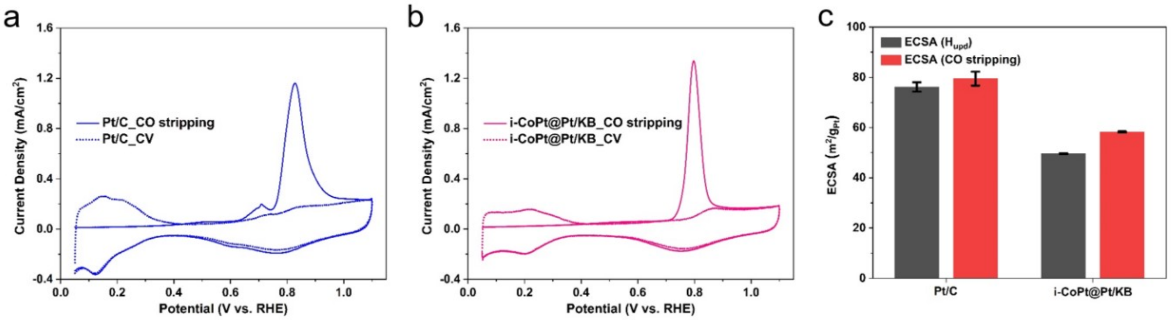

Figure S22. CO stripping curves of (a) Pt/C and (b) i-CoPt@Pt/KB. (c) ECSA of Pt/C and i-CoPt@Pt/KB calculated from H_{upd} and CO stripping.

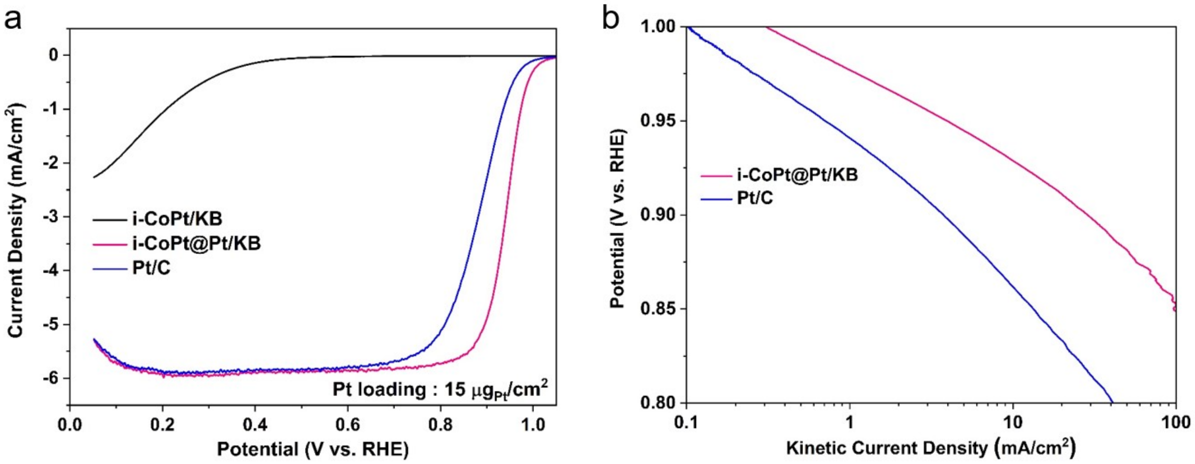

Figure S23. (a) ORR polarization curves and (b) Tafel plots of i-CoPt@Pt/KB compared to i-CoPt/KB and Pt/C.

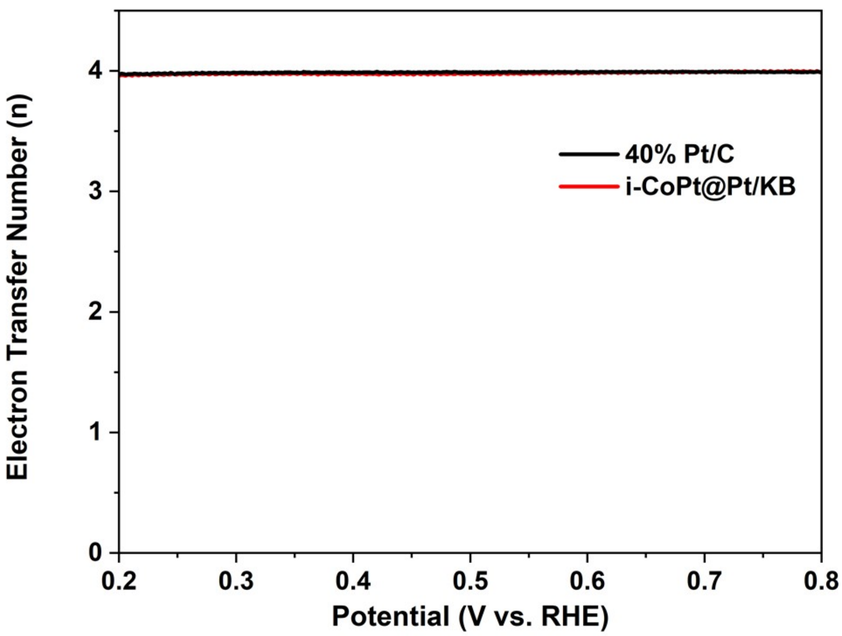

Figure S24. Electron transfer numbers of i-CoPt@Pt/KB and commercial Pt/C calculated by rotating ring-disk electrode measurement.

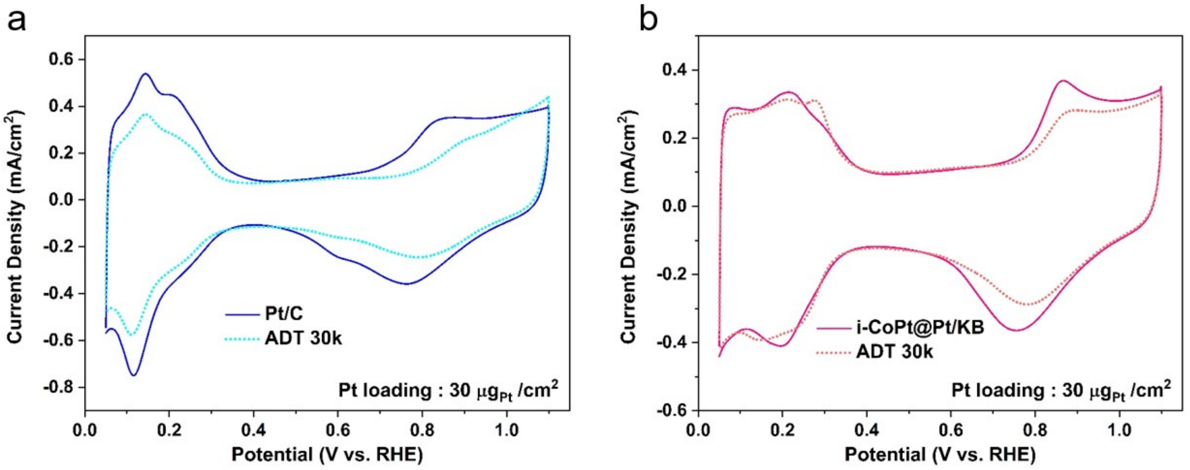

Figure S25. CV curves of (a) Pt/C and (b) i-CoPt@Pt/KB before and after ADT for 30,000 cycles.

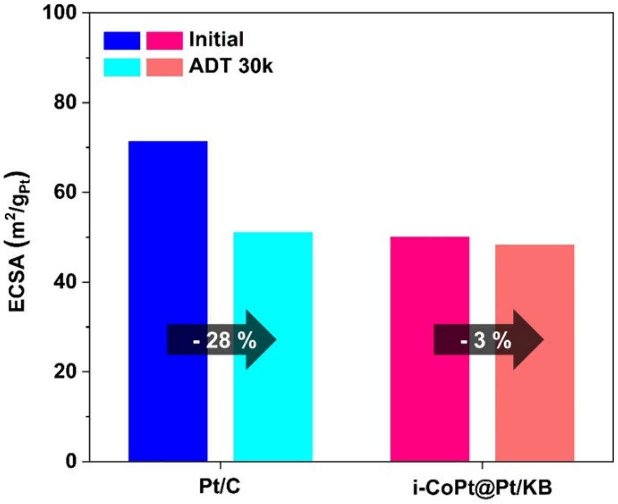

Figure S26. ECSA (H_{upd}) of Pt/C and i-CoPt@Pt/KB before and after ADT for 30,000 cycles.

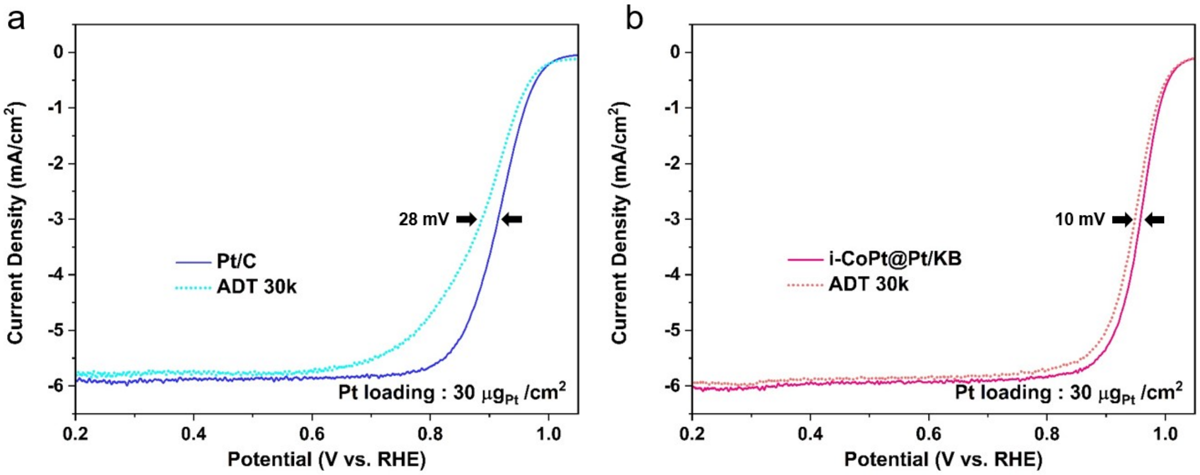

Figure S27. ORR polarization curves of (a) Pt/C and (b) i-CoPt@Pt/KB before and after ADT for 30,000 cycles.

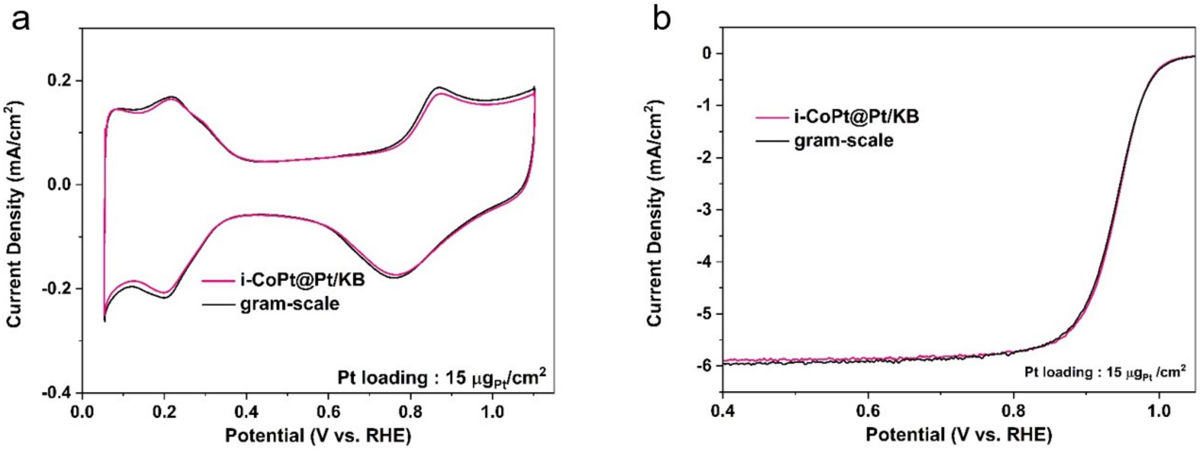

Figure S28. (a) CV curves and (b) ORR polarization curves of i-CoPt@Pt/KB and its gram-scale synthesis sample.

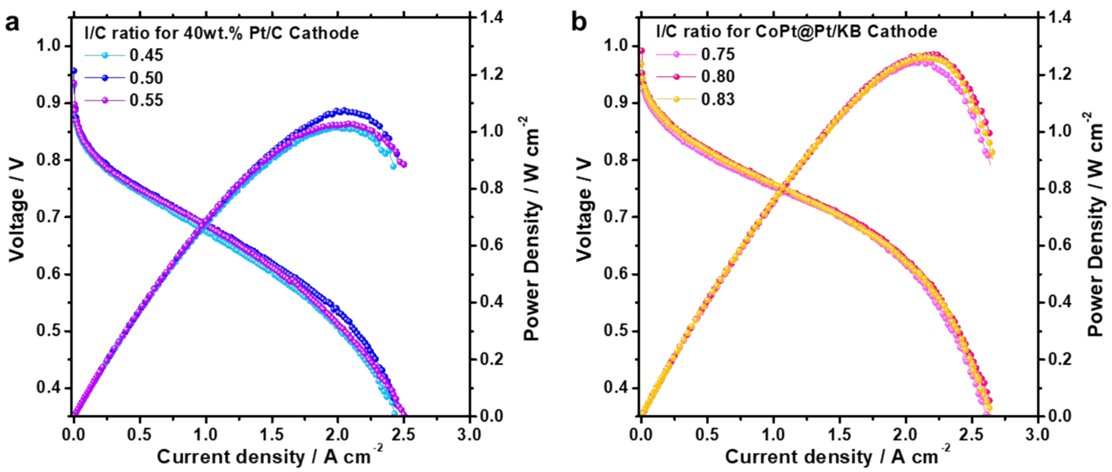

Figure S29. Optimization of ionomer to carbon ratios (I/C) on H_2-air fuel cell performance for (a) Pt/C and (b) i-CoPt@Pt/KB.

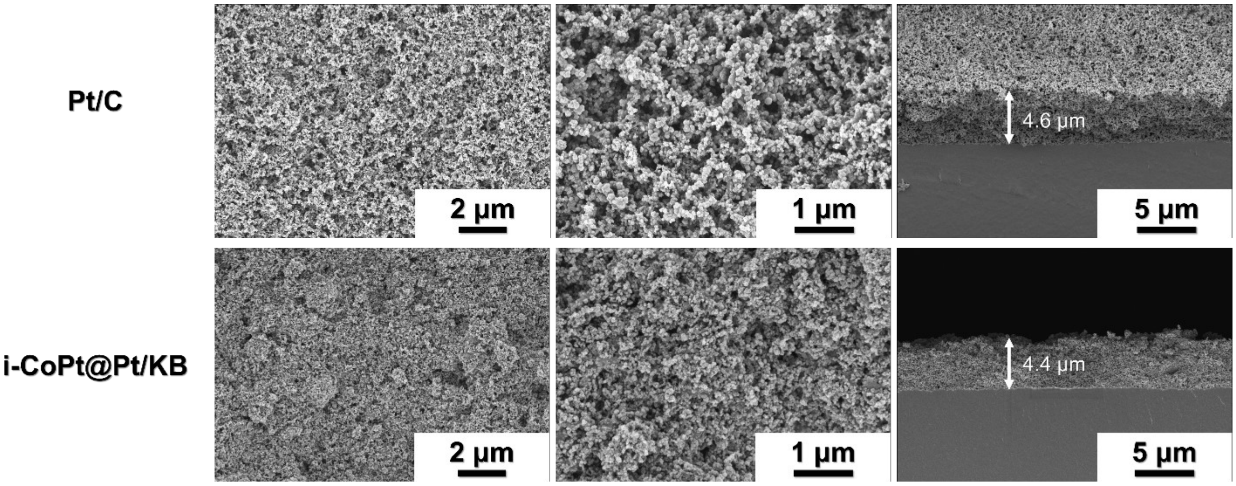

Figure S30. SEM images of CCLs of both CCMs (Pt/C and i-CoPt@Pt/KB) by top-view and cross-section observation.

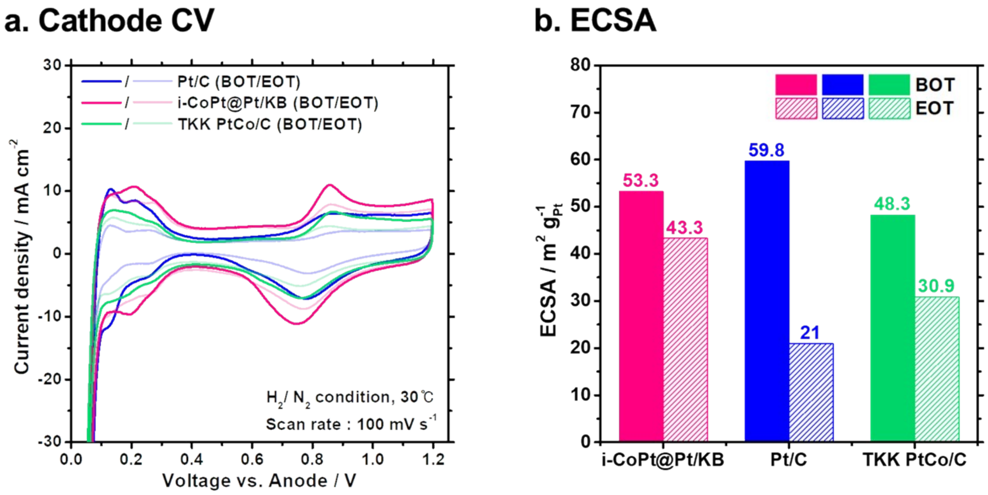

Figure S31. (a) CV curves, and (b) ECSA values of i-CoPt@Pt/KB, benchmark Pt/C, and benchmark TKK PtCo/C cathodes in MEA configuration before and after ADT cycling. Test condition (H_2-N_2): 30 °C, 100% relative humidity, H_2 flow rate = 0.2 L min^{-1}, N_2 flow rate = 0.2 L min^{-1}.

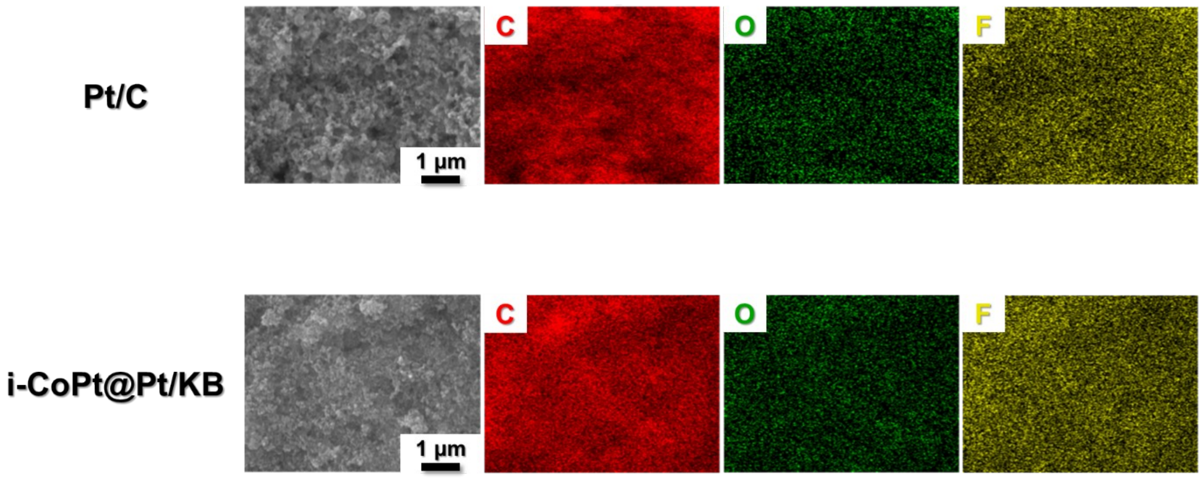

Figure S32. SEM-EDS mapping data of CCLs of Pt/C and i-CoPt@Pt/KB MEAs.

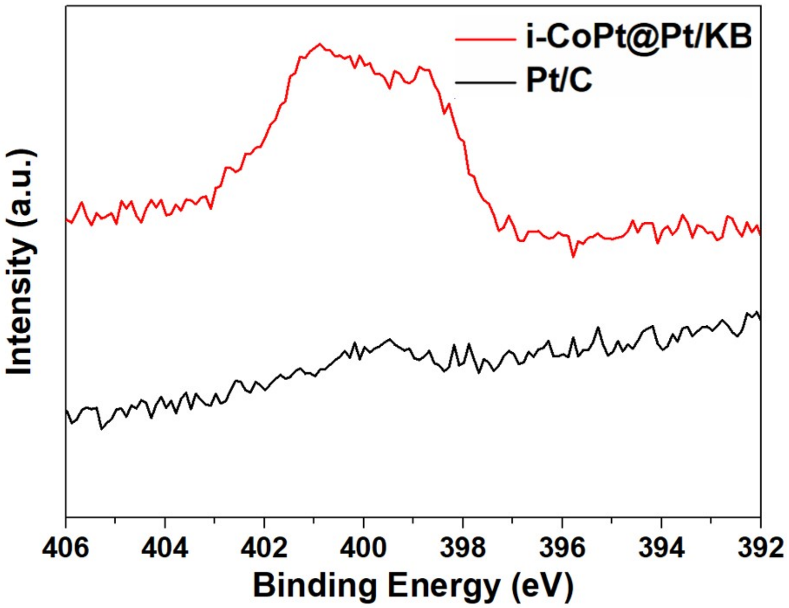

Figure S33. XPS N 1s spectra of Pt/C and i-CoPt@Pt/KB.

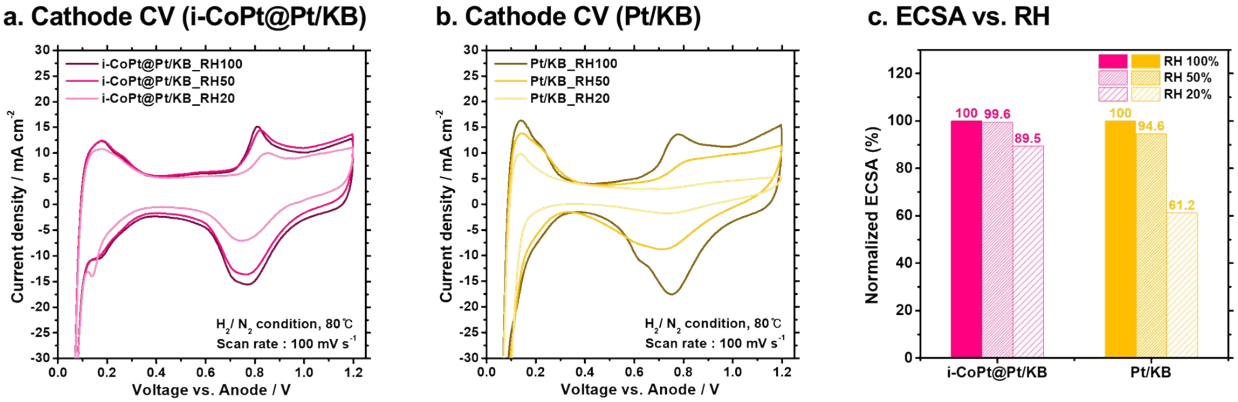

Figure S34. CV curves of (a) i-CoPt@Pt/KB, and (b) Pt/KB at various relative humidity (RH, 100%, 50%, and 20%) (c) Normalized ECSA versus relative humidity. Test condition (H_2-N_2): 80 °C, H_2 flow rate = 0.2 L min^{-1}, N_2 flow rate = 0.2 L min^{-1}.

Supporting Description: To demonstrate that the N-doped carbon surface of i-CoPt@Pt/KB is beneficial for the homogeneous ionomer distribution in CCL, we prepared a KB-based catalyst without N-doped carbon surface (denoted as Pt/KB) and fabricated the MEA with this Pt/KB (ionomer to carbon weight ratio was 0.8, equivalent to i-CoPt@Pt/KB cathode). To evaluate the ionomer distribution and its coverage over the two KB-based CCLs (i-CoPt@Pt/KB and Pt/KB), ECSA was measured as a function of relative humidity (100, 50, and 20%) at 80 °C. Under a dry condition, proton conduction is possible only to the Pt surface adjacent to ionomer, so the normalized ECSA at low RH (20%) to the ECSA at 100% RH indicates the coverage of the ionomer and its proximity to a catalyst particle. As shown in **Figure S34c**, i-CoPt@Pt/KB cathode revealed much higher normalized ECSA (89.5%) than Pt/KB cathode (61.2%) under 20% RH condition. We can conclude here that the much lower sensitivity of ECSA of i-CoPt@Pt/KB compared to that of Pt/KB is a result of a better distribution of ionomer and effective formation of triple phase boundaries in i-CoPt@Pt/KB cathode. Thus, the higher retention of ECSA in MEA configuration for i-CoPt@Pt/KB sample can be attributed to the N-doping on KB that could attract ionomer and prevent the detrimental coverage of Pt surface by ionomer.

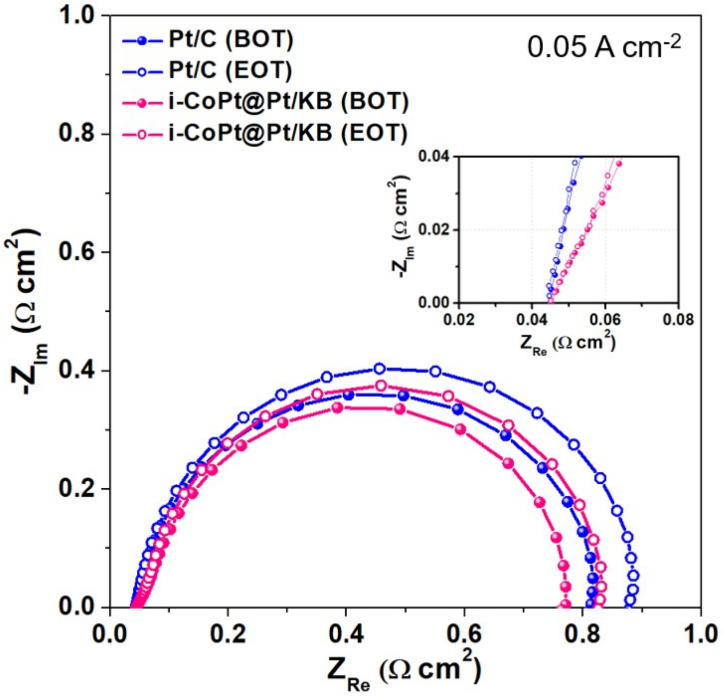

Figure S35. EIS at 0.05 A cm^{-2} of i-CoPt@Pt/KB and Pt/C at BOT and EOT.

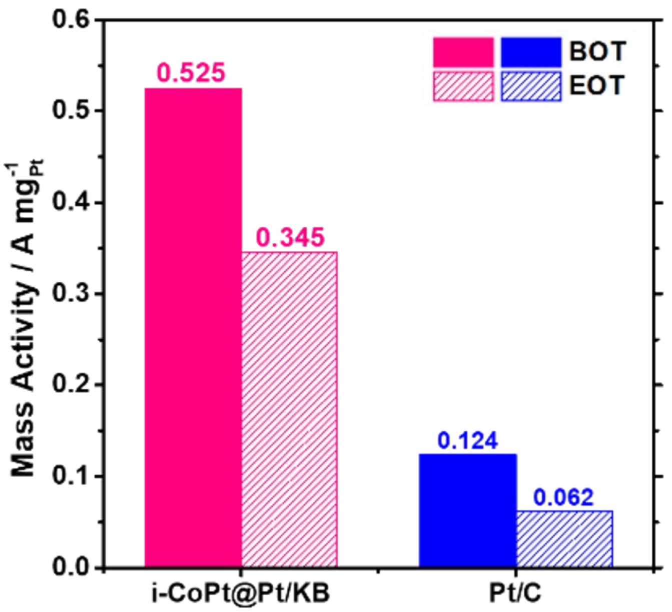

Figure S36. MEA cathode mass activities (at 0.9 V versus RHE) of i-CoPt@Pt/KB and Pt/C before and after ADT cycling.

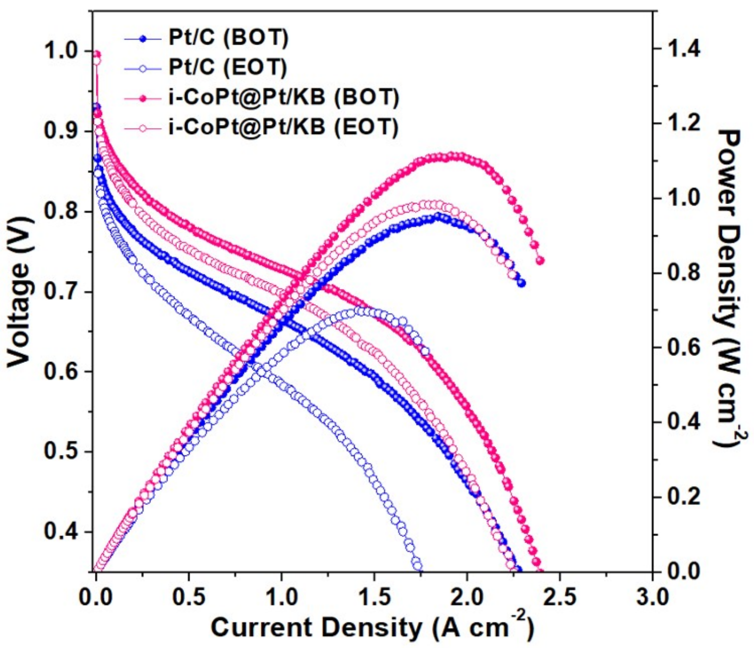

Figure S37. H_2-air fuel cell polarization and power density curves of i-CoPt@Pt/KB and Pt/C with 150 kPa$_{abs}$ at BOT and EOT.

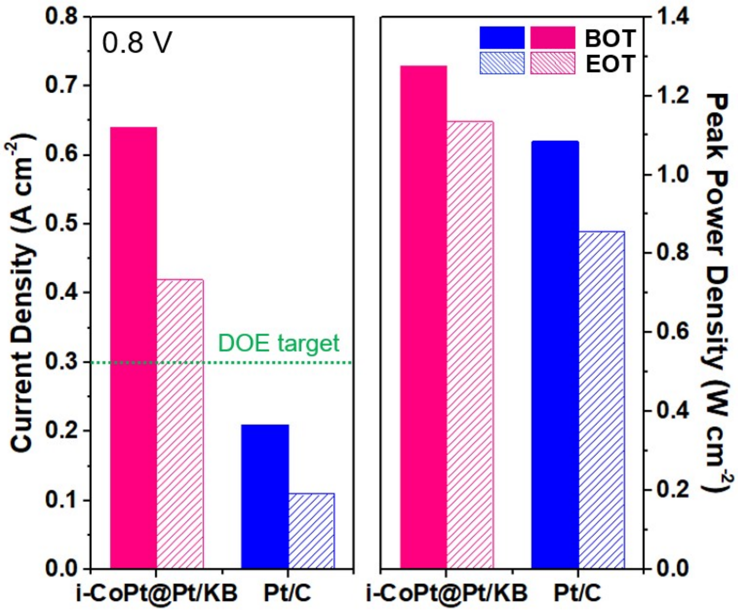

Figure S38. Current density at 0.8 V (left) and peak power density (right) of i-CoPt@Pt/KB and Pt/C at BOT and EOT.

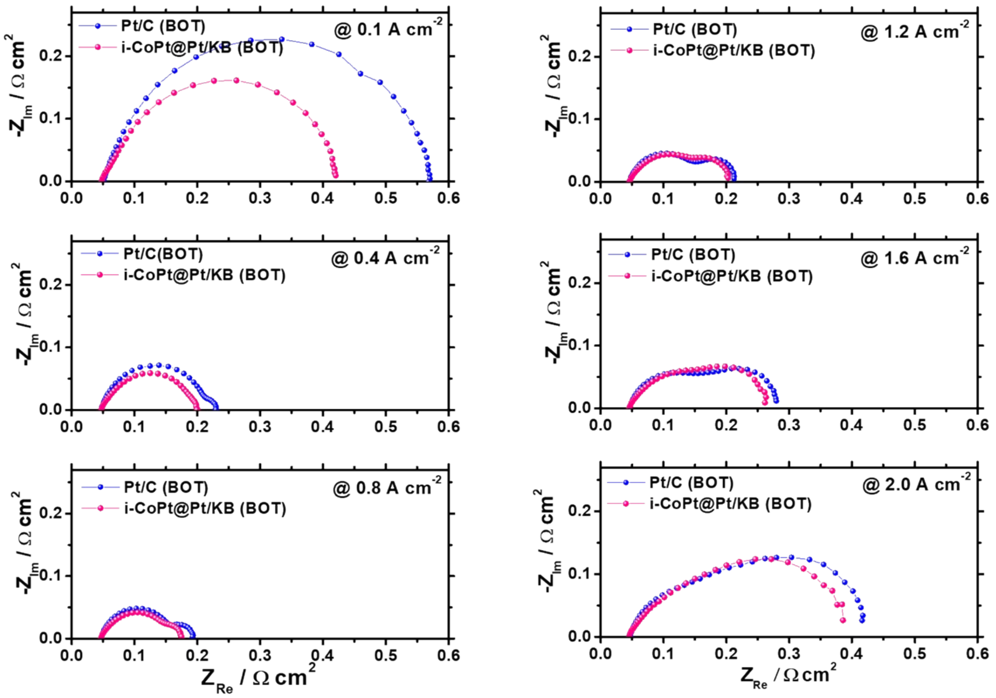

Figure S39. EIS spectra measured at various current densities (0.1 to 2.0 A cm^{-2}) of the i-CoPt@Pt/KB and the benchmark Pt/C under H_2-air condition. Test condition (H_2-air): 80 °C, 100% relative humidity, H_2 flow rate = 0.2 L min^{-1} (250 kPa$_{abs}$), air flow rate = 0.8 L min^{-1} (250 kPa$_{abs}$).

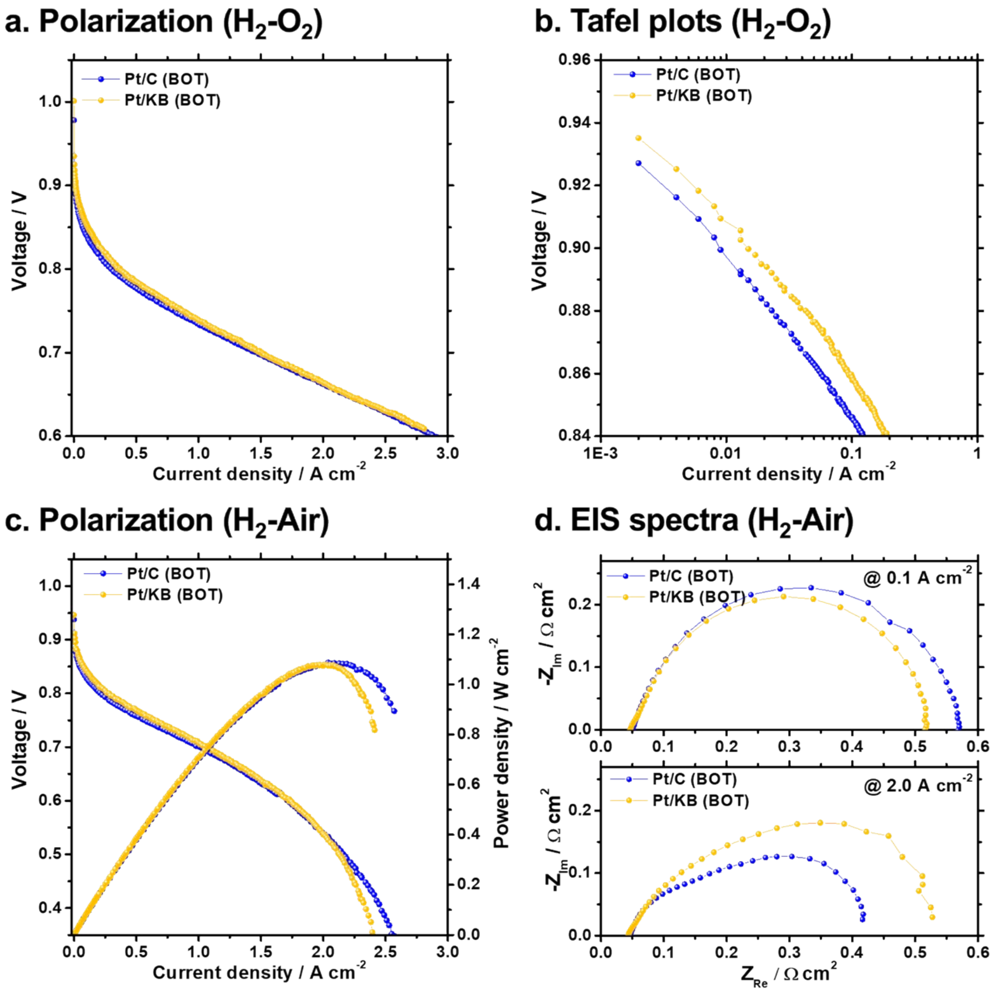

Figure S40. Single cell performance of the Pt/KB and the benchmark Pt/C under H_2-O_2 and H_2-air conditions. (a) H_2-O_2 fuel cell polarization curves and (b) the derived Tafel plots. Test condition (H_2-O_2): 80 °C, 100% relative humidity, H_2 flow rate = 0.2 L min^{-1} (150 kPa$_{abs}$), O_2 flow rate = 0.2 L min^{-1} (150 kPa$_{abs}$) (c) H_2-air fuel cell polarization curves and (d) EIS spectra at 0.1 A cm^{-2} and 2.0 A cm^{-2}. Test condition (H_2-air): 80 °C, 100% relative humidity, H_2 flow rate = 0.2 L min^{-1} (250 kPa$_{abs}$), air flow rate = 0.8 L min^{-1} (250 kPa$_{abs}$).

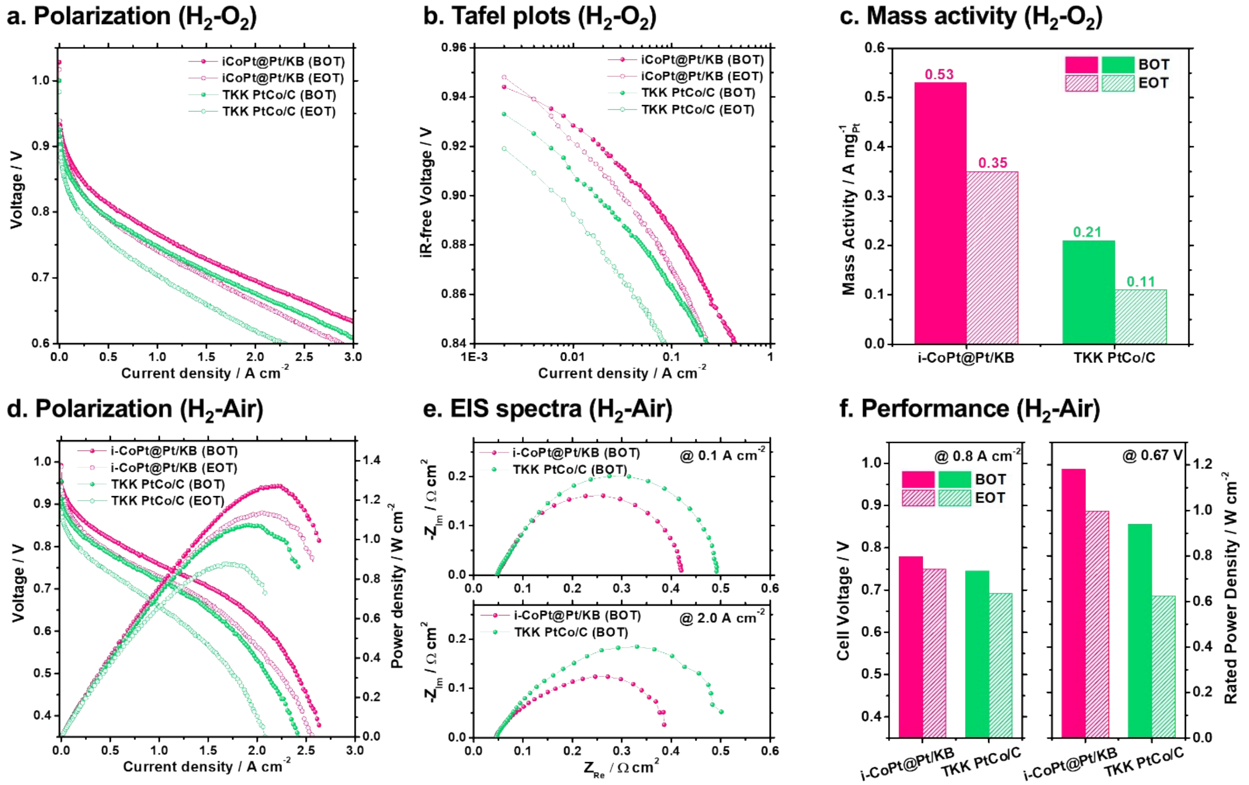

Figure S41. Single cell performance and durability of the i-CoPt@Pt/KB and the benchmark TKK PtCo/C under H_2-O_2 and H_2-air conditions. (a) H_2-O_2 fuel cell polarization curves and (b) the derived Tafel plots before and after ADT cycling. (c) ORR mass activities in MEA configuration. Test condition (H_2-O_2): 80 °C, 100% relative humidity, H_2 flow rate = 0.2 L min^{-1} (150 kPa$_{abs}$), O_2 flow rate = 0.2 L min^{-1} (150 kPa$_{abs}$) (d) H_2-air fuel cell polarization curves and (e) EIS spectra at 0.1 A cm^{-2} and 2.0 A cm^{-2}. (f) Cell voltage at 0.8 A cm^{-2} (left) and rated power density at 0.67 V (right). Test condition (H_2-air): 80 °C, 100% relative humidity, H_2 flow rate = 0.2 L min^{-1} (250 kPa$_{abs}$), air flow rate = 0.8 L min^{-1} (250 kPa$_{abs}$).

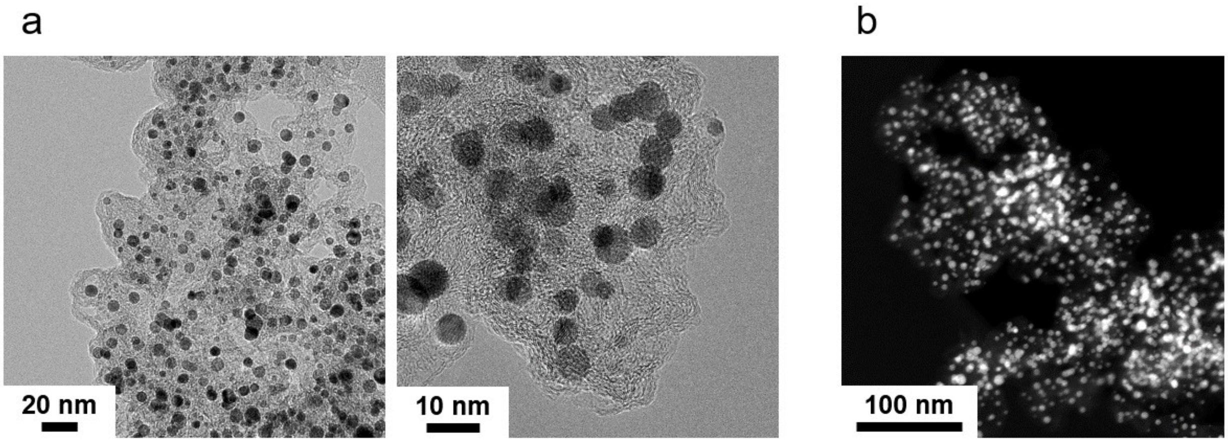

Figure S42. (a) TEM and (b) STEM images of i-CoPt@Pt/KB at EOT.

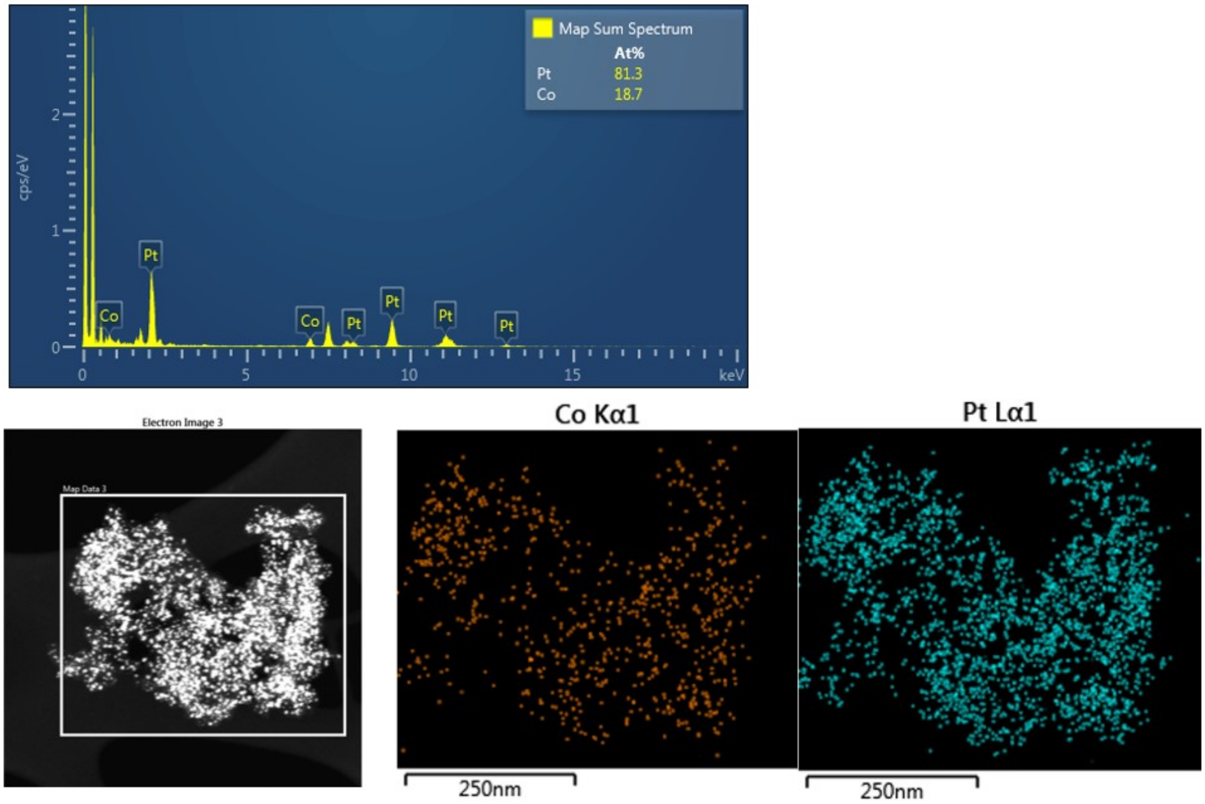

Figure S43. STEM-EDS spectrum and mapping of i-CoPt@Pt/KB at EOT.

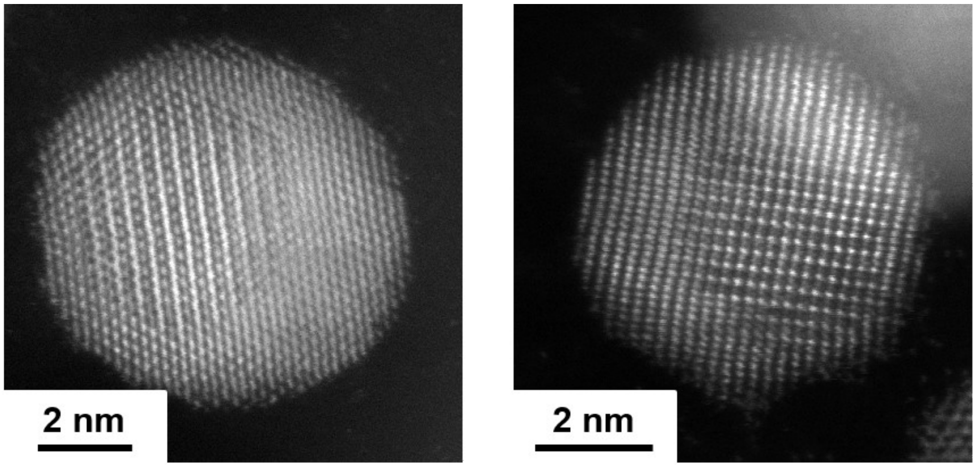

Figure S44. HAADF-STEM images of i-CoPt@Pt/KB at EOT.

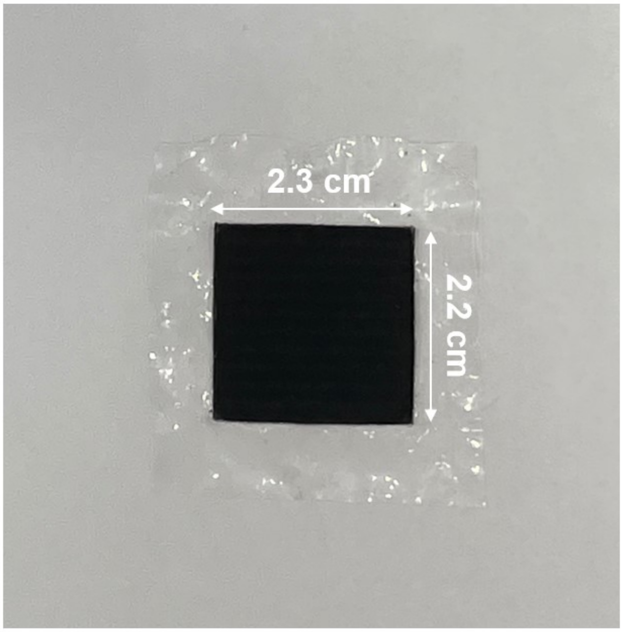

Figure S45. Photograph of the catalyst-coated membrane.

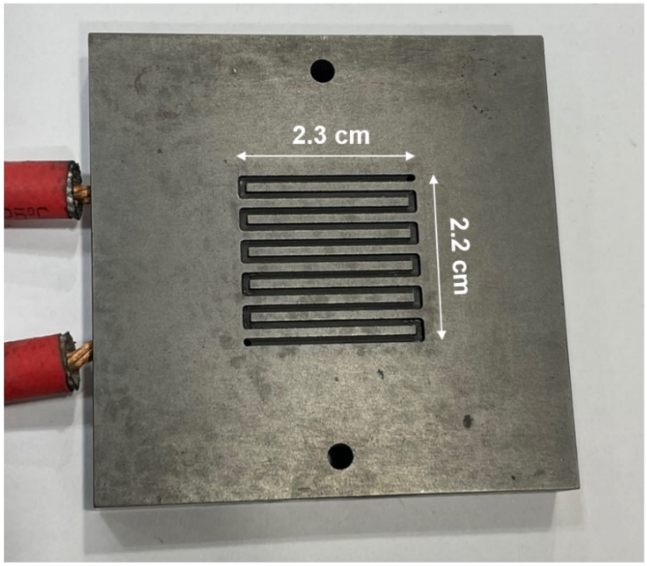

Figure S46. Photograph of the flow field.

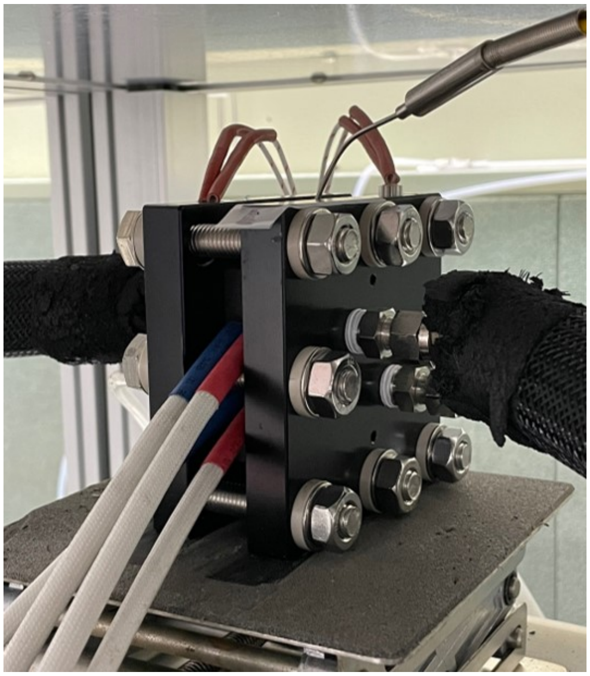

Figure S47. Photograph of the single cell configuration after assembly.

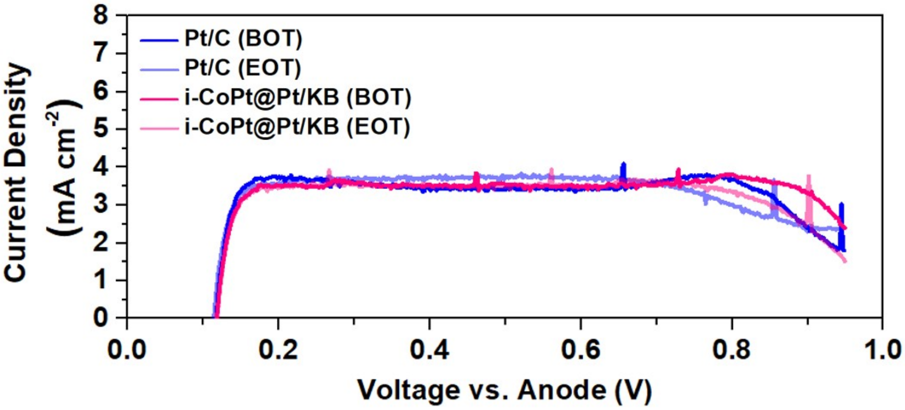

Figure S48. Hydrogen crossover currents of i-CoPt@Pt/KB and Pt/C at BOT and EOT.

Table S1. Co:Pt atomic ratios of Co-Pt compound measured by STEM-EDS at three different sites.

EDS site	Atomic Co : Pt
#1	49.7 : 50.3
#2	49.8 : 50.2
#3	50.9 : 49.1

Table S2. Co:Pt atomic ratios and the Pt mass loadings of i-CoPt/KB and i-CoPt@Pt/KB, measured by ICP-AES.

Sample	Atomic Co : Pt	Pt mass loading (wt %)
i-CoPt/KB	46.87 : 53.13	28.71
i-CoPt@Pt/KB	28.38 : 71.62	40.05

Table S3. Comparison of Pt loading, MEA mass activity in H_2-O_2 condition, and MEA power performance of i-CoPt@Pt/KB in H_2-air condition compared with the state-of-the-art Pt-alloy catalysts in literature.

Catalyst	Anode Pt loading ($mg_{Pt}\ cm^{-2}$)	Cathode Pt loading ($mg_{Pt}\ cm^{-2}$)	Outlet Pressure (kPa_{abs})	H_2/O_2 Flow Rate ($L\ min^{-1}$)	Cathodic Mass Activity @ 0.9 $V_{iR\text{-}free}$ ($A\ mg_{Pt}^{-1}$)	H_2/Air Flow Rate ($L\ min^{-1}$)	Current Density @ 0.8 V ($A\ cm^{-2}$)	Rated Power Density @ 0.67 V ($W\ cm^{-2}$)	Specific Power @ 0.67 V ($W\ mg_{Pt}^{-1}$)	Reference
i-CoPt@Pt/KB	0.1	0.1	150	0.20/0.20	**0.53**	0.20/0.80	**0.37**	**1.02**	**5.1**	**This work**
			250	-	-		**0.64**	**1.18**	**5.9**	
Pt/C	0.1	0.1	150	0.20/0.20	0.12	0.20/0.80	0.11	0.65	3.25	This work
			250	-	-		0.20	0.84	4.2	
LP@PF-2	0.35	0.033	150	0.20/0.20	1.77	0.20/0.52	0.27	0.65	1.69	*1*
			250	-	-		0.27	0.75	1.95	
PtNi-BNCs/C	0.1	0.15	300	-	-	0.15/0.30	0.53	0.82	3.28	*3*
$L1_0$-CoPt/Pt	0.1	0.105	150	0.50/1.00	0.56	0.50/1.00	0.26	0.60	2.93	*4*
$L1_0$-W-PtCo/C	0.1	0.11	150	0.20/0.20	0.57	0.20/0.50	0.29	0.51	2.43	*5*
Pt_3Co/FeN_4-C	0.1	0.1	150	0.50/1.00	0.72	0.50/1.00	0.355	0.824	4.12	*6*
Pt1Co1-IMC@Pt/C	0.1	0.2	200	1.00/0.40	0.18	1.00/1.50	0.28	0.943	3.14	*7*

References

1. L. Chong, J. Wen, J. Kubal, F. G. Sen, J. Zou, J. Greeley, M. Chan, H. Barkholtz, W. Ding and D.-J. Liu, Ultralow-loading platinum-cobalt fuel cell catalysts derived from imidazolate frameworks. *Science*, 2018, **362**, 1276-1281.
2. S. H. Lee, J. Kim, D. Y. Chung, J. M. Yoo, H. S. Lee, M. J. Kim, B. S. Mun, S. G. Kwon, Y.-E. Sung and T. Hyeon, Design Principle of Fe–N–C Electrocatalysts: How to Optimize Multimodal Porous Structures? *J. Am. Chem. Soc.*, 2019, **141**, 2035-2045.
3. X. Tian, X. Zhao, Y.-Q. Su, L. Wang, H. Wang, D. Dang, B. Chi, H. Liu, E. J. M. Hensen, X. W. Lou and B. Y. Xia, Engineering bunched Pt-Ni alloy nanocages for efficient oxygen reduction in practical fuel cells. *Science*, 2019, **366**, 850-856.
4. J. Li, S. Sharma, X. Liu, Y.-T. Pan, J. S. Spendelow, M. Chi, Y. Jia, P. Zhang, D. A. Cullen, Z. Xi, H. Lin, Z. Yin, B. Shen, M. Muzzio, C. Yu, Y. S. Kim, A. A. Peterson, K. L. More, H. Zhu and S. Sun, Hard-Magnet $L1_0$-CoPt Nanoparticles Advance Fuel Cell Catalysis. *Joule*, 2019, **3**, 124-135.
5. J. Liang, N. Li, Z. Zhao, L. Ma, X. Wang, S. Li, X. Liu, T. Wang, Y. Du, G. Lu, J. Han, Y. Huang, D. Su and Q. Li, Tungsten-Doped $L1_0$-PtCo Ultrasmall Nanoparticles as a High-Performance Fuel Cell Cathode. *Angew. Chem. Int. Ed.*, 2019, **58**, 15471-15477.
6. Z. Qiao, C. Wang, C. Li, Y. Zeng, S. Hwang, B. Li, S. Karakalos, J. Park, A. J. Kropf, E. C. Wegener, Q. Gong, H. Xu, G. Wang, D. J. Myers, J. Xie, J. S. Spendelow and G. Wu, Atomically dispersed single iron sites for promoting Pt and Pt_3Co fuel cell catalysts: performance and durability improvements. *Energy Environ. Sci.*, 2021, **14**, 4948-4960.
7. Q. Cheng, S. Yang, C. Fu, L. Zou, Z. Zou, Z. Jiang, J. Zhang and H. Yang, High-loaded sub-6 nm Pt1Co1 intermetallic compounds with highly efficient performance expression in PEMFCs. *Energy Environ. Sci.*, 2022, **15**, 278-286.